Apatite Chemistry and Zoning in the Roseau Valley, Dominica, Lesser Antilles

****

By

Katherine Swager

Submitted in partial fulfillment of the requirements for the degree of Bachelor of Science

Department of Geology

UNION COLLEGE

June 2017

ABSTRACT

The island of Dominica is located in the center of the Lesser Antilles island arc. Located in the southwestern part of the island, the Roseau Valley contains a thick and complex stratigraphy of pyroclastic flows that terminate in the sea on the western side of the island near the capital of Roseau, likely originating from the Wotten Waven caldera, now partially capped by the Micotrin dome (Sigurdsson, 1972). We have dated several ignimbrite deposit using U-Th analyses of zircon rims. The ages of five deposits within the valley show polymodal distributions, suggesting multiple periods of crystallization (~6 ka - 250 ka). The youngest deposit at Casso and an ignimbrite on the eastern side of the island near Rosalie, have distinctive zircon populations. The relationship between these deposits and the underlying magma chamber are poorly understood. The whole-rock chemistry of deposits throughout the valley is similar, and ranges from 58-65 wt% SiO_2. Apatite crystals from five pumice clasts were analyzed by BSE, CL, elemental mapping, and laser ablation ICP-MS. The crystals were ~35-50 μm in length and did not exhibit any zoning in BSE. Most crystals showed zoning in CL, suggesting differences in REE and/or trace element chemistry. Zoning patterns show “streaky” CL in two samples and three other samples have grains with irregularly shaped cores. The “streaky” crystals also have cores enriched in chlorine and rims enriched in fluorine. This may have implications for pre-eruption magma chamber conditions, as recent work suggests apatite may record volatile saturation as an eruption trigger (Boyce and Hervig, 2008; Stock et al., 2016). The apatite laser ablation and textural data showed the samples have distinctive compositions and histories. In one sample, the apatites have significantly higher oxygen fugacity, LREE/HREE ratios, and darker cores than the other samples, but have similar silica content and chronology to other samples, showing that the differences in apatite chemistry cannot be due to fractional crystallization processes. The grains with irregular cores contain slightly lower Sr/Y ratios, and may be inherited cores from the incorporation of non-erupted residual material as new melts ascend.

Overall the apatite textures and chemistry are variable between samples, suggesting the different eruptive events originate from chemically distinct magma and have unique ascent paths and crystallization histories. This work further suggests that there is not one large magma chamber beneath Dominica, but numerous semi-related bodies supplying magma to the surface with the potential for transient vertical connectivity (Cashman et al, 2017). The most recent reactivation of the Micotrin volcanic center in the past 6 ka may have been caused by a mafic injection, triggering an eruption resulting in the RI-13 andesitic pyroclastic deposit.

ACKNOWLEDGEMENTS

I would like to extend my sincerest thanks to my thesis advisor, Holli Frey. Her passion, and enthusiasm drove this project and helped me to realize my own interests in the field of volcanology. Her encouragement also helped me to be more confident in my abilities as a student and a scientific researcher. I would also like to thank Matt Manon for the helping me with technical aspects of this project, including spending many hours with me on the SEM.

I would also like to thank the entire geology department faculty for their encouragement, support, and wisdom throughout my time here. I would like to especially thank Anouk Verheyden-Gillikin for being my academic advisor throughout my time at Union.

I would like to thank my geology peers and friends who have been with me every step of the way. A special thanks to everyone who came to Dominica, it is a trip I will never forget. Finally, I would like to thank my family for supporting me and encouraging me to explore and make the most of my time at Union.

TABLE OF CONTENTS

Abstract ii
Acknowledgements iv
Table of Contents v
List of Figures vi
List of Tables vii
Appendix viii
Introduction 1
    Geologic Setting 1
    Location Descriptions 8
        St. Aromant (RI-9) 8
        Trafalgar (RI-10) 8
        Casso (RI-13) 9
        King’s Hill (KH-4) 10
        Rosalie (RI-15) 10
    Apatite in Volcanic Systems 13
        Apatite Fingerprinting 13
        Interpretation of Magmatic Processes 14
        Volatiles in Apatite 16
Methods 22
    Bulk Rock Chemistry 22
    Apatite Mineral Separation 22
    LA ICP-MS 23
    Scanning Electron Microscope 23
Results 24
    Bulk Rock Geochemistry 24
    Cathodoluminescence Zoning 30
    Elemental Mapping 34
    Single Apatite Grain Chemistry 38
    Comparison of Whole Rock and Apatite Chemistry 42
    Comparison of Zircon Chronology and Apatite Chemistry 45
    Oxygen Fugacity 46
Discussion 48
    The Single Source Hypothesis 48
    Apatite Chemistry and Magmatic Processes 50
    Interpretation of Apatite Textures 53
    Chlorine-Fluorine Zoning and Magmatic Processes 55
    Proposal of Multiple Magma Batches 56
Conclusions 59
References 61
Appendix 65

LIST OF FIGURES

Figure 1: Map of the Lesser Antilles island arc and geologic map of Dominica.
Figure 2: 2002 shallow seismic swarms partially beneath Micotrin Dome.
Figure 3: Hazard map in the event of a dome-forming eruption from Micotrin.
Figure 4: Zircon population density plots for deposits in this study.
Figure 5: Field image of St. Aromant (RI-9).
Figure 6: Field image of Trafalgar Falls (RI-10).
Figure 7: Field image of Casso (RI-13).
Figure 8: Field image of Rosalie (RI-15).
Figure 9: Sample location map.
Figure 10: Apatite as a monitor for pre-eruptive volatile saturation.
Figure 11: Relative stratigraphic position of eruptive deposits and their silica content.
Figure 12: Whole rock geochemistry of Al_2O, CaO, K_2O, Fe_2O_3 vs. SiO_2.
Figure 13. Whole rock geochemistry of MgO, Na_2O, Sr, Ba vs, SiO_2.
Figure 14. Rare earth element curve for Roseau deposits.
Figure 15. Cathodoluminescence apatite zoning and categories.
Figure 16. RI-9 apatite crystal elemental maps for F, Cl, Al, Ca, S, and Si.
Figure 17. Chlorine and fluorine zoning of RI-9 apatite.
Figure 18. Comparison of cathodoluminesence zoning and Cl/F zoning in RI-10.
Figure 19. Ce/Lu vs. Sr/Y of individual apatite grains.
Figure 20. La/Nd vs. Sm/Dy of individual apatite grains.
Figure 21. Whole rock SiO_2 vs. apatite Sr.
Figure 22. Whole rock Sr vs. apatite Sr.
Figure 23. Relative stratigraphy of samples and apatite Yb/Dy composition.
Figure 24. Model of a homogeneous batholith beneath Dominica from Smith et al. (2013).
Figure 25. Model of RI-13 ascent path and origin of irregular cores.
Figure 26. Vertical model of a magma storage system.

LIST OF TABLES

Table 1: Cathodoluminescence textural categories of apatite samples.
Table 2: Occurrence of chlorine and fluorine zoning in apatite samples.
Table 3: Oxygen fugacity values for southern Dominica samples.

APPENDIX

Table 1. Whole rock geochemistry, major oxides (wt. %) and trace elements (ppm), concentrations.
Table 2. Whole rock rare earth element concentrations in ppm.
Table 3. Single apatite grain rare earth element concentrations in ppm with Sr/Y, Ce/Lu, La/Nd, Yb/Dy, and Sm/Dy ratios.

INTRODUCTION

Geologic Setting

The island of Dominica is located at the eastern edge of the Caribbean and at the center of the Lesser Antilles Island arc. This chain of volcanic islands is a product of the subduction of the North American tectonic plate beneath the Caribbean plate. The plates converge at a rate of ~2 cm/year. The arc can be segmented into two parts; the northern part trends at 330° and the southern part trends at 020°. This change is accompanied by a 10-30° increase in slab dip from the north to the southern portion of the arc (Wadge and Shepherd, 1984, Howe et al., 2015). Dominica is located at the southern end of the northern portion (Figure 1).

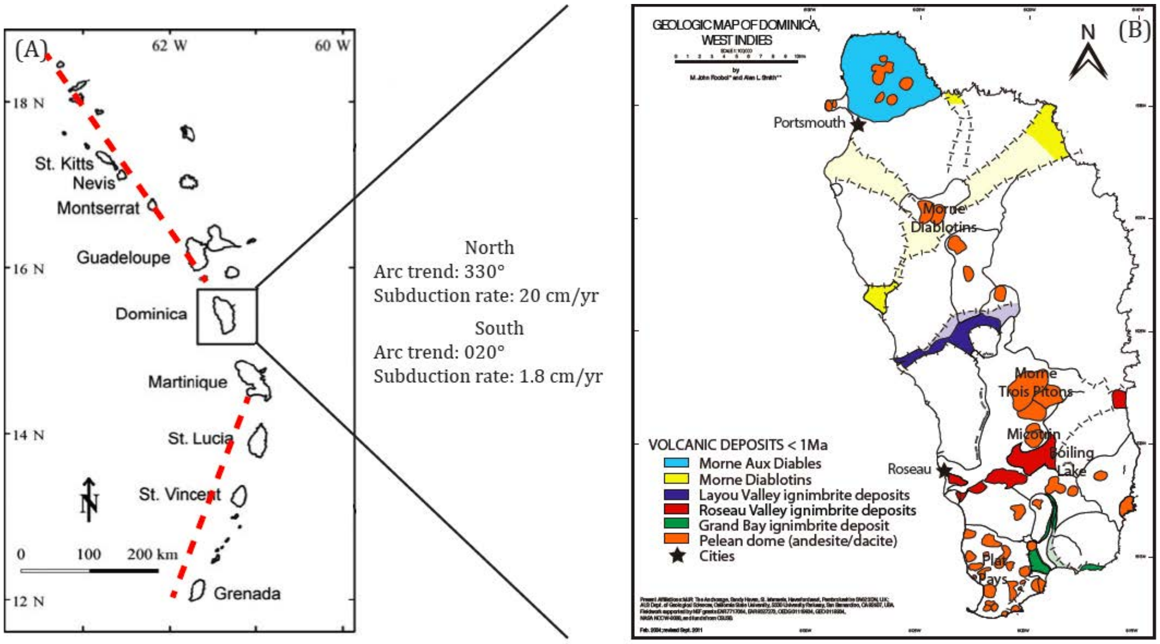

Figure 1. (A) Dominica is situated in the center of the Lesser Antilles island arc, at a point where there is a change in the arc trend and subduction rate (map from Lindsay et al.,2005) (B) A geologic map of Dominica showing pyroclastic flow deposits radiating from their associated lava domes (map from Smith et al., 2013; modified by Brehm, 2015).

Dominica contains at least 9 volcanic centers, whereas the rest of the Lesser Antillean islands only have 1 or 2 (Lindsay et al., 2005). The island is composed almost entirely of andesitic volcanic rocks, with the exception of the discontinuous Pleistocene shoreline conglomerates, coral, and limestone deposits along the west coast (Sigurdsson and Carey, 1991) and the Foundland basalt in the southeast dated at ~2.3 Ma (Bellon, 1988). The highly weathered basal portion of the island is composed of basaltic and andesitic breccia and lavas, and their ages are estimated to range from the Eocene to Pliocene (Martin-Kaye, 1960). The oldest whole rock ages on the island are dated to 7 Ma by K-Ar (Smith et al., 2013). Older zircons up to billions of years old have been found, but they are detrital (Frey, unpublished).

The active, modern volcanism started in the Pleistocene, and is composed of andesite/dacite volcanoes forming lava domes (Lindsay et al, 2005). The mountainous spine of the island is composed of these lava domes, and associated deposits radiate from these peaks, including block and ash flows, pyroclastic flow deposits, and air-fall deposits. Today, there are numerous potentially active volcanic centers on the island, as there are active geothermal fields (Traineau et al., 2015) and the island has frequently experienced shallow seismic swarms (Seismic Research Unit 2000). The only eruptions to occur in historical times were phreatic eruptions from the Valley of Desolation in 1880 and 1997 (Lindsay et al., 2003). In the Pleistocene, there have been multiple large-volume pyroclastic flows (Carey and Sigurdsson, 1972; Sigurdsson, 1980). One of these deposits is named the Roseau Ignimbrite, which once filled the valley that is now being excavated by the Roseau River, and is home to the capital city of Dominica, which has a population of ~17,000 people.

The Seismic Research Unit (2000) published an eruption hazard evaluation for Dominica, and they found reason to be concerned for a potential eruption from the Micotrin Dome. Radiocarbon dating of pyroclastic deposits at Laudat, adjacent to Micotrin Dome, yielded ages at ~26,000 and 1,160 years. They interpreted this as the reactivation of the volcanic center after a period of quiescence. Seismic swarms partially beneath the Micotrin Dome and the Roseau valley in 2002 have also suggested this center has the potential to reactivate (Lindsay et al, 2002; Figure 2). Lindsay et al. (2005) recognized the potential hazard for a dome-forming eruption from Micotrin and created a hazard map. The entire southern portion of the island would be at risk for hazards, since pyroclastic flows from Micotrin have the potential to flow both east and west (Lindsay et al., 2005; Figure 3).

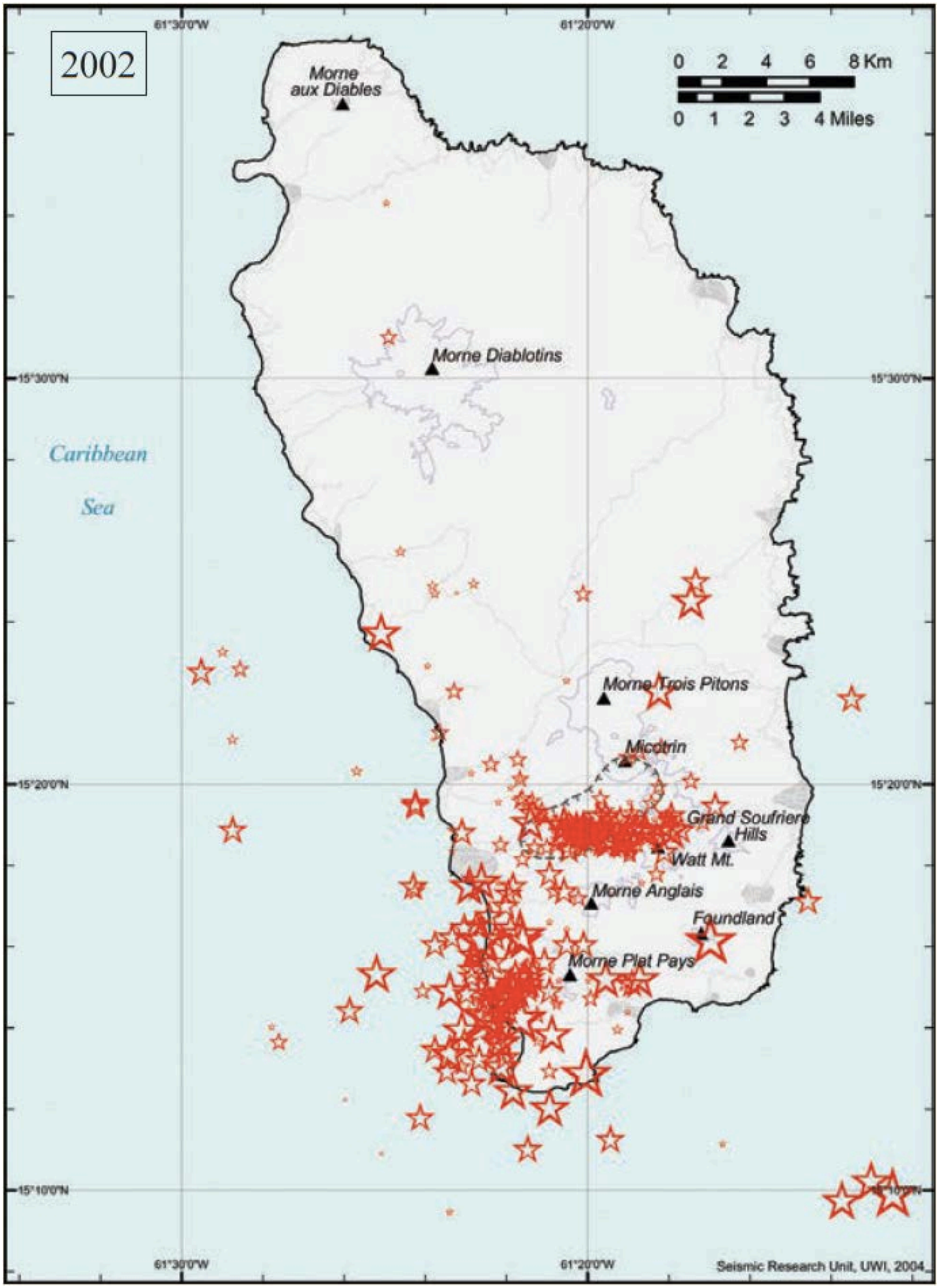

Figure 2. Map of 2002 shallow seismic swarms on Dominica, which were partially beneath Micotrin Dome and the Roseau Valley (Lindsay et al., 2005).

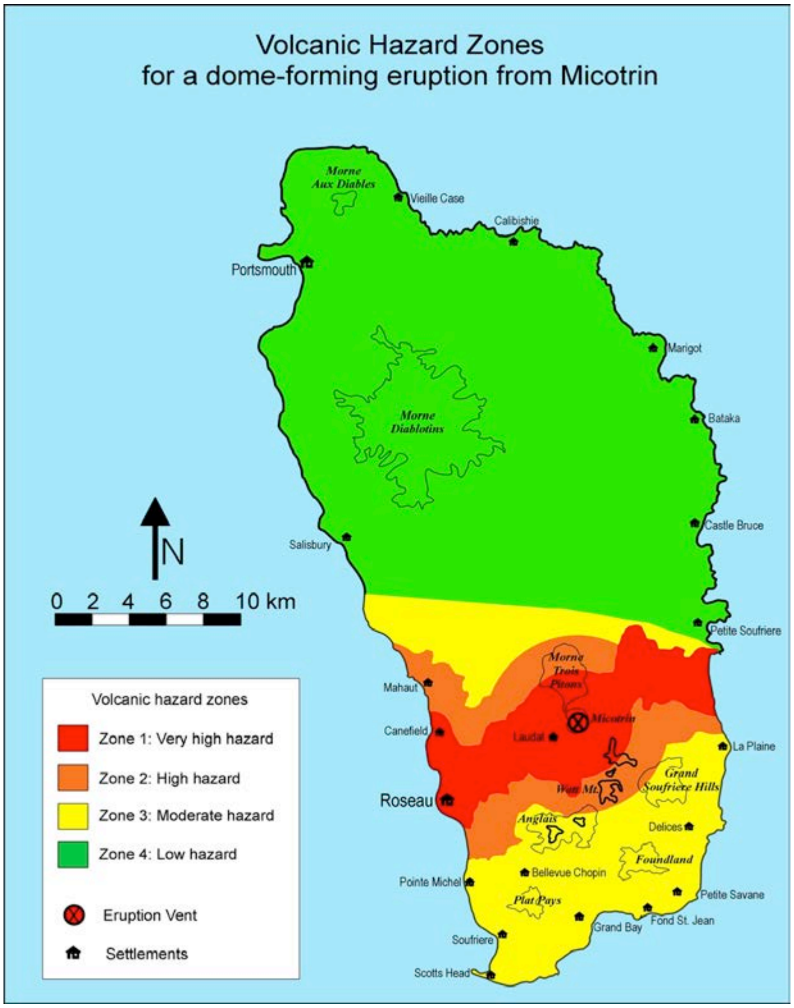

Figure 3. Hazard map in the event of a dome-forming eruption from the Micotrin volcanic center (Lindsay et al., 2005).

The Roseau Ignimbrite was previously thought to originate from one large eruption based on work by Sigurdsson (1972) and Carey and Sigurdsson (1980). The similar glass and mineral chemistry of deposits recovered from off-shore cores suggested that all of this material was erupted from one source, likely the Wotten Waven caldera, now occupied by the Micotrin Dome, potentially in one large eruption (Sigurdsson, 1972). Although Sigurdsson (1972) found multiple paleosols separating the deposits, his further studies estimated that >58 km^3 of material was erupted, making this eruption the largest in the Caribbean in the last 200,000 years (Carey and Sigurdsson, 1980).

However, further studies have proposed that the Roseau ignimbrite is the product of up to 7 smaller eruptions (Smith et al., 2013, Howe et al., 2014), and the off-shore deposits may be due to a combination of eruptions from other centers (Smith, et al., 2013). Radiocarbon ages from the Goodwill Quarry ignimbrite sequence span from 26,380 +/- 190 to >46 ka (Lindsay et al., 2005, Carey and Sigurdsson, 1980). Howe et al. (2014) compared these ages to (U-Th)/He ages and found that there was a larger age range that previously thought, and explosive eruptions occurred between 24-80 ka. Although geochemical and petrographic analyses are similar for different eruptions, the Roseau Ignimbrite described by Carey and Sigurdsson (1980) was split into at least six smaller eruptions based on ages by Howe et al. (2014).

The origin and extent of the deposits that comprise the Roseau ignimbrite are an ongoing debate. Based on proximity, the Wotten Waven caldera is the source of the eruptions, partially buried by the Micotrin dome (Sigurdsson, 1972; Demange et al., 1985; Lindsay et al., 2005; Smith et al., 2013). Howe et al., (2014) proposed that the Goodwill Quarry, along with the Link Flow locations, all originated from a single magma source due to their similar whole-rock, glass, and mineral geochemistry, and this source is likely Micotrin/Wotten Waven. The volcanic deposits at the Wall House Quarry, just south of the Roseau Valley, were previously correlated to the Morne Anglais volcano due to the similarity of charcoal ages to scoria deposits at Anglais (Lindsay et al, 2005). The pyroclastic deposits at Wall House Quarry have also been correlated to the Grand Bay ignimbrite by Lindsay et al. (2003) due to overlapping whole rock chemistry. Later, they were attributed to the Roseau Ignimbrite by Smith et al. (2013) due to mineralogical and topographical constraints. It remains unclear the relationship between the Roseau and

Grand Bay Ignimbrites, as well as the origin of the Wall House Quarry deposits (Howe et al., 2014). The eruption and deposit ages of the Roseau Ignimbrite show a long and varying history. Howe et al. (2014) found that the Roseau eruptive sequence spanned 6 events between 20 to 80 ka using U-Th/He zircon dating. However, new research by the Frey group has found an ignimbrite deposit at Casso as young as 3+/-8 ka using U-Th zircon rims (Figure 4). Along with the 26,00 and 1,160 ^{14}C age at Laudat (Seismic Research Unit, 2000), there appears to be a gap in eruptive activity from the Micotrin center from roughly ~20-6 ka.

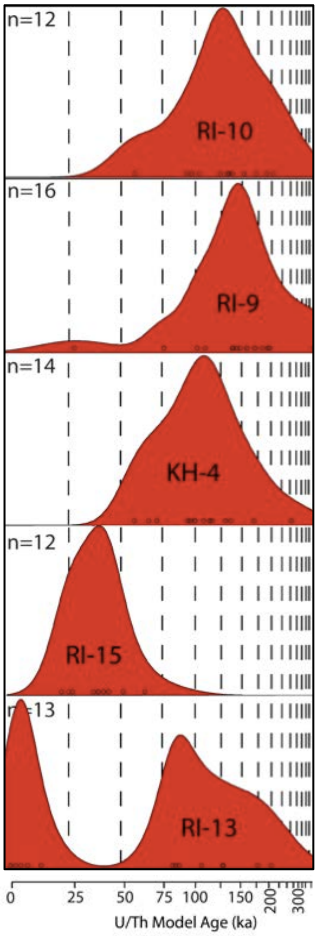

Figure 4. Zircon U-Th rim ages plotted by probability-density. The zircon ages for RI-9, RI-10, and KH-4 are similar, whereas RI-15 and RI-13 are much younger. RI-13 has an older age (bimodal), which may suggest multiple periods of crystallization. (Figure from Frey et al., 2016).

Location Descriptions

St. Aromant (RI-9)

This ignimbrite unit is the stratigraphic base of Link road, termed Link Flow 1 by Howe et al. (2014). It is 20 meters thick and is clast-supported by crystal-rich pumice ranging from 1 to 20 cm. The pumice is dense and had low vesicularity. The ignimbrite is lithic poor, containing 1% lithics. The sample was taken at the bottom of the ignimbrite deposit (Figure 5).

Figure 5. St. Aromant (RI-9) ignimbrite is 20 meter thick, and the sample was taken at the bottom of the unit, just above the ash lens at the bottom of the deposit.

Trafalgar (RI-10)

Trafalgar Falls is located along the Roseau River in the Trois Pitons National Park (Figure 6). There are large blocks up to 2-3 meters of welded tuff. Some blocks contain elongate fiamme (3-8 cm), the samples are crystal rich, and also large lithics up to 8-10 cm. The samples are also slightly pink, indicating weathering and/or oxidation. (Adapted from Brehm, 2015).

Figure 6. At Trafalgar Falls, large blocks of welded tuff (RI-10) were dislodged after Tropical Storm Erica in August of 2015.

Casso (RI-13)

The sample was taken near the top of the ignimbrite deposit, as the bottom of the deposit was water-saturated. The deposit has a sugary texture, but is more cemented and less weathered at the top, as the pyroxenes were still black and retained their elongate shape. This deposit is ash-rich, and contains small (1-5 cm) semi-welded pumice clasts. This outcrop was lithic rich, with 10% angular blocks ranging from 1-10 cm. The welding of the pumice showed us that the flow dips to the west at 15-30° (Figure 7).

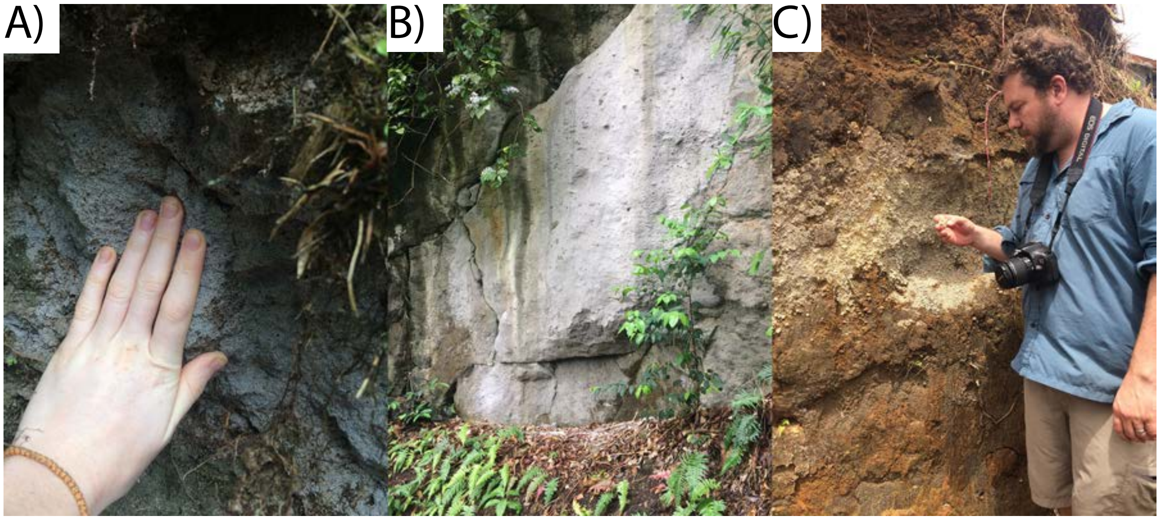

Figure 7. Casso Estate (RI-13) A: The sugary texture near the bottom of the ignimbrite. B: The welded pumice of RI-13 at the top of the ignimbrite. C: RI-16, an unconsolidated air fall deposit of ash and lithics near the top of the ridge.

King’s Hill (KH-4)

This ~20 m high outcrop was accessed by walking down Jack’s Walk Trail. There were multiple units in this cliff outcrop, and KH-4 was collected from the upper 13 m of the outcrop. KH-4 is somewhat lithified and has unconsolidated pumice clasts of 5 to 15 cm. (adapted from Flake, 2014).

Rosalie (RI-15)

RI-15 is located in the Rosalie river valley on the east coast. This ~5 m high outcrop is unconsolidated and contains crystal-rich, fairly-vesicular, grey-white pumice clasts (Figure 8). Some clasts are large, >40 cm, however most are ~10 cm. Some lithics are present, lithic to pumice ratio is ~7:3. The outcrop has been mapped as part of the Roseau ignimbrite, emanating from Wotten Waven (Smith et al., 2013) and is the only known ignimbrite in eastern Dominica. (Adapted from Babiak, 2016).

Figure 8. A 5 meter high ignimbrite (RI-15) collected from the eastern side of the island near the town of Rosalie with pumice clasts up to 40 cm large (Photo from Babiak, 2016).

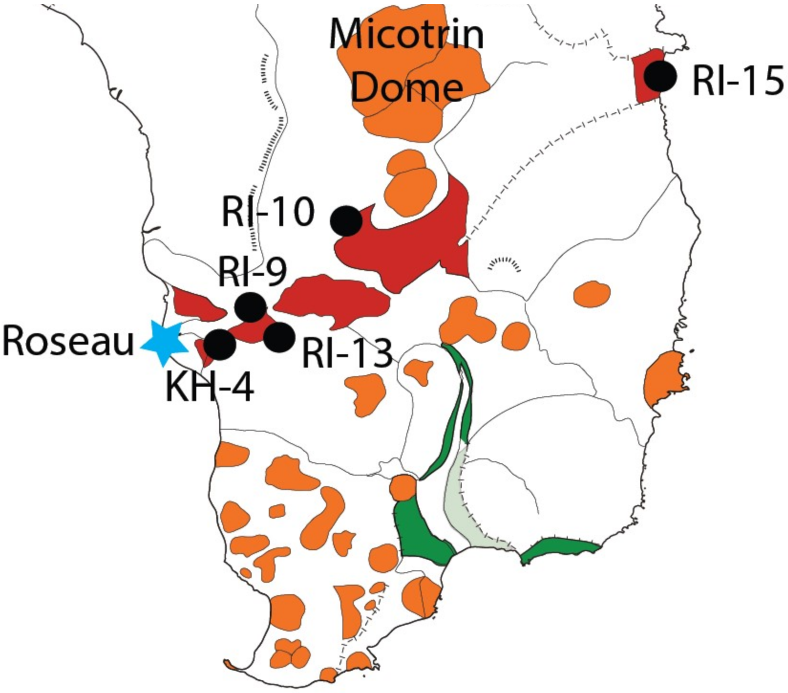

Figure 9. Map of sample locations in the Roseau Valley and near Rosalie (RI-15). Orange represents lava domes, while the green (Grand Bay) and red (Roseau) represent pyroclastic flows. Adapted from Brehm et al. (AGU Poster).

Apatite in Volcanic Systems

Apatite refers to three end-member compositions of the mineral; chlorapatite, fluorapatite, and hydroxylapatite, with the chemical formula $Ca_5(PO_4)_3(F,Cl,OH)$. Apatite can contain more than half of the elements on the periodic table, and REE can substitute into the calcium site. Apatite occurs in two crystal habits: equant and acicular. Equant apatite is interpreted to have formed at near-equilibrium conditions. Acicular apatite grows under conditions far from equilibrium and rapid cooling. The extent of apatite occurrence along with its diverse and flexible compositions leads it to have many applications in the field of volcanology and petrology.

Apatite is an accessory mineral that occurs in almost all rocks on earth. Most research on apatite is directed to the exploration of ore bodies. It is a phosphate mineral and constitutes much of the sedimentary rock phosphorite, which is mined for fertilizer. Apatite also has important applications for analyzing and understanding volcanic systems, and more research is needed to understand its full potential. Ultimately, the study of apatite could lead to a better understanding of the evolution of magma bodies and mechanisms of volcanic systems. For example, apatite can record a change in volatile content abruptly prior to eruptions (Stock et al., 2016).

Apatite Fingerprinting

The chemical composition of apatite makes it helpful in distinguishing volcanic deposits. This is because its crystal structure has sites that can host different sized atoms available for substitutions (Hughes and Rakovan, 2015). A method called ‘apatite fingerprinting’ has been used to map the extent of explosive deposits or K-bentonites, which are ash beds that have undergone alterations (Shaw, 2003). This involves the dissolution and chemical analysis of single apatite grains, which may have distinctive rare earth element compositions related to their magmatic origin. Apatite is more resistant to alterations during this process than matrix glass or other phenocrysts, and as the whole ‘rock’ composition is altered, apatite will reflect the original ash composition allowing bentonite beds to be distinguished (Samson et al., 1998). Analyzing apatite populations within the bentonite layers gives statistical data on their variability, which can be used to assess the possibility for regional correlation or even multiple events within the bed (Shaw, 2003). Apatite ‘finger printing’ can help to understand the extent and periodicity of past volcanic eruptions. Ash beds, or tephra, are important markers within the geologic record. Thus, apatite also has applications in tephrachronology (Sell and Samson, 2011).

Interpretation of Magmatic Processes

Rare earth elements in apatite are useful beyond fingerprinting and tephrachronology. Their varying abundance in apatite crystals reflects the conditions within the magma chamber from which it crystallized. Early studies of the relationship between apatite and the melt composition used the crystal composition compared to the rock matrix. However the matrix of volcanic rocks is usually heterogeneous and the rare earth elements are difficult to measure (Prowatke and Klemme, 2006). Experiments have been essential in determining apatite and melt partitioning relationships. Initial experiments showed that REE and Sr are strongly compatible in apatite within silicate melts (Watson and Green, 1981). Further experimentation by Prowatke and Klemme (2006) yielded apatite/melt partition coefficients that strongly agreed with the findings of Watson and Green (1981), and can help to explain general trends in the REE signature of apatite. The REEs substitute for Ca in the crystal structure, which has a similar ionic radius to the middle REEs, explaining why they partition more strongly than the heavy or light REE. It was also shown that the partitioning of REEs into the crystal structure increases with melt polymerization and evolution. Their experiments at a range of magma compositions yielded partition coefficients that can be applied to natural apatite. Other factors of the melt were found to affect the partitioning of REE into apatite. The oxidation state of the reservoir can affect the REE distribution because elements such as Ce and Eu are sensitive to oxygen fugacity, and experiments have shown higher fO_2 correlate with higher Eu and Ce (Watson and Green, 1981; Roeder et al., 1987).

The trace elements incorporated into the apatite structure can be especially helpful in interpreting magma or fluid and the petrogenetic processes it has undergone (Harlov, 2015; Webster and Piccoli, 2015). Trace and REE zoning within apatite can reflect changes in the melt composition. In plutonic rocks, Tepper and Kuehner (1999) found complex BSE zoning due to abrupt changes in REE, Y, and Si content of apatite crystals in a batholith, and correlated these patterns between apatite grains. The possible origins of zoning are inherited cores, element diffusion rates, co-precipitation of REE-rich minerals, or magma mixing. They determined that magma mixing and differentiation was the only plausible explanation for the zoning of these crystals, besides inheritance, which could not be ruled out. The presence of resorption textures, abrupt compositional changes, and a lack of systematic core to rim chemical variation in the apatite crystals are characteristic of mixed volcanic rocks. They stated that the growing crystals could have moved through compositionally heterogeneous melt domains to create this complex zoning.

Inherited cores can also cause trace element zoning within apatite. Demster et al. (2003) investigated the nature of inherited cores within a granite intrusion. They found texturally discernable cores in CL with chemistry more variable than mantles of the crystals. Some cores had dissolution textures, so they hypothesized that these cores previously crystallized, had been partially dissolved, and later acted as a nuclei for further growth. These inherited cores can be useful when deciphering magmatic evolution, however it highlights the need for caution when interpreting geochemical signatures of apatite when dissolving whole grains (Demster et al., 2003).

Zoning of REEs within apatite may be at concentrations too low to be imaged with BSE. Cathodoluminesence imaging can be used to expose zoning within the crystals. Luminescence within apatite crystals is due to impurity elements that act as activators (Roeder et al., 1987). These impurities are the REEs that substitute into the structure. The main activators in apatite are Mn^{2+}, Sm^{3+}, Dy^{3+}, Tb^{3+}, Eu^{2+}, and Eu^{3+}.

Volatiles in Apatite

Monitoring gaseous emissions from volcanoes has proven to be a valuable tool in predicting eruptions and monitoring long-term emissions from volcanoes (Boyce and Hervig, 2008; Scott et al., 2014; Tepper and Keuhner, 1999). Volatiles in a magma chamber can affect the pressurization within the magma chamber. Exsolution and replenishing of volatiles in a magma chamber can over-pressurize the magma chamber and trigger an eruption. Typically, melt inclusions have been used to estimate volatile contents in a pre-eruptive melt, but inclusions can be vulnerable to post-entrapment leakage or bubble growth, which changes their compositions. Some geologists have proposed that apatite may serve as a better monitor of volatile compositions in the melt

(Stock et al., 2016). Apatite takes up and can substitute all major volatiles (OH, C, S, Cl, F) into its crystal structure. The uptake of these volatile components into apatite depends on the melt composition, the presence of other halogen-bearing minerals, and the pressure temperature conditions (Zhu and Sverjensky, 1991). Volatile abundance in a crystallizing mama chamber can have implications for magmatic processes and eruption potential.

In igneous systems, apatite volatile compositions have been used to estimate the long term degassing of a magma chamber in the absence of gas emissions monitoring (Scott et al., 2014). Changes in the volatile composition of a melt are recorded in the chemical zoning of apatite as it grows in changing conditions. Complex zoning can create chemical stratigraphy throughout a crystal showing the evolution of volatile contents before an eruption. Boyce and Hervig (2008) used a secondary ion mass spectrometer (SIMS) to measure the proportions of chlorine, fluorine, and water at 5 μm intervals along the traverse of a crystal. Some crystals contained unique volatile stratigraphies, suggesting that the crystals were at different depths during magmatic recharge events. However, there were some discernable patterns between the grains they analyzed, which had homogenous OH-rich cores, and rims that became progressively enriched in Cl, with dramatic oscillations in OH content, and little change in F. This was interpreted as a product of degassing of H_2O and recharge of volatile-rich magma in the magma chamber.

A timescale was modeled based on diffusion rates, and assumed pressure and temperature of the chamber, estimating that these crystals and their zoning were developed ~400 days prior to the eruption, at temperatures of ~800°C (Boyce and Hervig, 2008). At higher pressures, this timescale could be reduced to just a few days. This has implications for the progression of volatile composition and trigger of eruptions, as an increasing frequency and intensity of volatile degassing and recharge events directly preceded the eruption.

Stock et al. (2016) used a different method to determine the pre-eruption volatile history of magma of crystals from Campi Flagrei. Using secondary ion mass spectrometry and electron microprobe analysis, they measured fluorine, chlorine, and water in apatite crystals, which they determined to be in different stages of magma evolution. They used apatite phenocrysts, along with microphenocrysts within other minerals, such as clinopyroxene or biotite, which crystallized at different pressure/temperature ranges prior to eruption. The apatite crystals within different minerals recorded the volatile composition during the crystallization period of the host mineral. They found that clinopyroxene and biotite hosted apatite inclusions contained a higher $X_{halogen}/X_{OH}$ value than apatite microphenocrysts which were in contact with the melt until eruption. They found H_2O content to be constant in the clinopyroxene phase (~2 wt%) but highly variable in the biotite phase (1.3-4.5 wt%). The matrix glasses had low H_2O content (<1 wt%) and halogen content similar to the biotite inclusions. Plots of the X_F/X_{OH} vs. X_{Cl}/X_{OH} compositions of different phases show a volatile-undersaturated trajectory. The H_2O content of the matrix glass indicates that the melt became H_2O saturated prior to the eruption. Figure 10 summarizes the timescale of the different mineral phases.

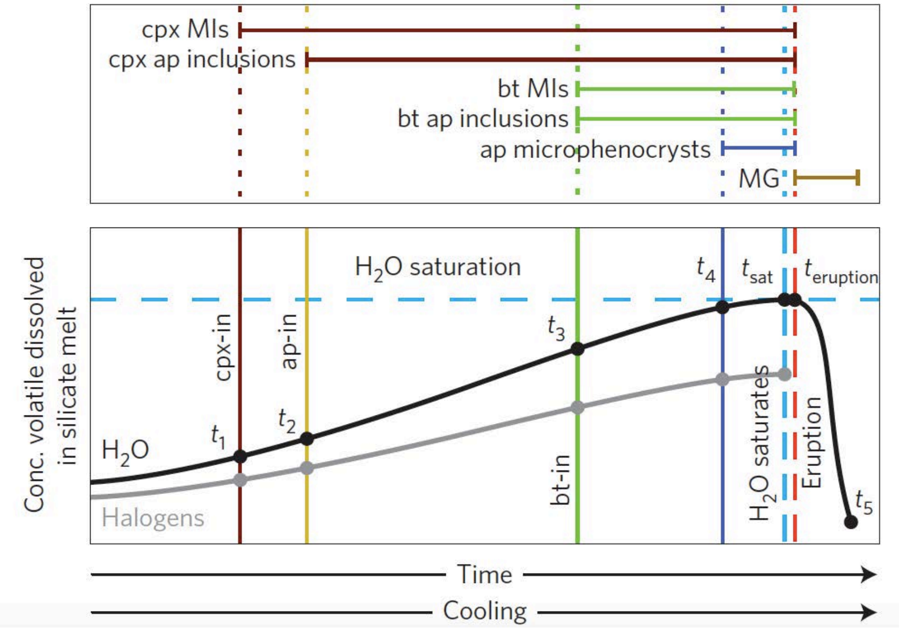

Figure 10. This chart summarizes the volatile and water content of the melt prior to eruption of Campi Flagrei, from Stock et al. (2016).

Since the volatiles within apatite show very little diffusion even when they were stored at high temperatures, the melt must have remained volatile-undersaturated until shortly before the eruption, on an order of 10-10^3 days. This may suggest that some restless volcanoes may erupt with little to no warning due to the recharge of volatiles. In restless systems such as Campi Flagrei, where magma storage conditions are volatile under-saturated, and explosive eruptions occur with little geodetic warning, the chemical monitoring of hydrothermal systems and fumerolic gasses can provide pre-eruptive indicators.

Similarly to Boyce and Hervig’s (2008) study, apatite volatile stratigraphy shows the pre-eruptive behavior of volatiles in a magma chamber can change on potentially short timescales of days to months. However, these timescales remain uncertain due to the diffusive behavior of volatiles within apatite crystals at varying temperatures and pressures, which are not well known. While Stock et al. (2016) found one abrupt H_2O

degassing event prior to eruptions, Boyce and Hervig (2008) found multiple events of H_2O degassing and volatile recharge during magma storage. This again highlights the need to further understand under what conditions volatile enrichment primes volcanoes for eruption.

This research shows how apatite can be an important tool in understanding the evolution of magma, and the volatile behavior in the melt prior to an eruption. However, there can be analytical difficulties in the measurement of volatile concentrations within apatite crystals. Stormer et al. (1993) determined that there is a variation in the F and Cl x-ray intensity at different crystallographic orientations of the crystal. Stock et al. (2015) confirmed that this is due to the implantation of electrons in the crystal on the c-axis, which causes the halogens to diffuse in response to the electric field. This effect is most pronounced on the c-axis due to diffusion along crystallographic sites in the c-axis channel. This poses analytical challenges to the accurate measurement of halogens within apatite.

The study of volcanic apatite presents numerous opportunities to unravel magma chamber dynamics and crystallization histories. Furthermore, apatite can give insight into volcanic volatile processes that may precede eruptions (Stock et al., 2015, Boyce and Hervig, 2008). Studies on the zoning of apatite in particular have not been utilized to their full potential. This study on the island of Dominica, Lesser Antilles uses apatite rare earth element chemistry, and cathodoluminescence zoning coupled with elemental mapping to illuminate magma chamber characteristics. Building on previous studies of apatite zoning and chemistry and zircon chronology, the findings of this study will aim to distinguish and understand numerous pyroclastic deposits on Dominica. The apatite characteristics will build on studies focused on the nature of the magma chamber beneath the island, whether the system is interconnected, or composed of smaller, independently crystallizing batches on magma, as well as providing another step towards understanding the eruptive potential of an understudied, volcanically active island.

METHODS

Adapted and summarized from Brehm, 2015

Bulk Rock Geochemistry

Pumice and lava samples were crusted in the hydraulic press and powdered by agitation in a Speck 15 cm aluminum oxide puck mill. The powders were send to Acme Labs, Vancouver, Canada and analyzed on an ICP-OES to obtain major elements and select trace elements (Ba, Sr, Zr, Y, Sc).

Trace element ICP-MS analyses at Union College were performed by weighing 200 mg of each powdered sample into a PicoTrace (Bovendan, Germany) Teflon bomb system. Four USGS standards were included (NIST-388, NIST-678, BIR-1, BCR-2). The samples were dissolved over a week-long process adapted by Hollocher et al. (2007) using HF, HNO_3, and HCl. The resulting solution was analyzed with a PerkinElmer Elan 6100 DRC ICP-MS

Apatite Mineral Separation

Pumice and lava samples were initially crushed to <2mm using a Jaw Crusher and a Bico Braun belt-driven pulverizer. The crushed rocks were decanted to remove pumice, glass, and low-density minerals. Magnetite crystals were removed using a free-fall hand magnet, and the sample was passed through tetrabromethane ($CHBr_2$) to separate higher density minerals. Then the samples were passed through a Franz magnetic separator to remove mineral phases. Finally, the heavy liquid methylene iodide was used to separate the resulting minerals. Apatites were handpicked under a stereographic microscope. These separates were mounted in epoxy resin and polished for SEM imaging and analysis.

LA ICP-MS

Apatites were analyzed using a Cetac frequency quintupled Nd: YAG laser with a wavelength of 213 nm connected to an ELAN 6100 DRC ICP, calibrated using NIST glasses 610 and 612 as standards. Apatite grains were ablated with a spot size of 25 µm at 100% laser power with a firing rate of 10 Hz. Helium was the carrier gas and combined with Ar gas to make a plasma. The elements analyzed included Sr, Y, La, Ce, Pr, Nd, Sm, Eu, Gd, Dy, Yb, Lu, Pb, Th, U.

Scanning Electron Microscope

Six carbon-coated apatite grain mounts were analyzed on the SEM. The samples were inserted into the chamber, and BSE images were taken of the mounts and stitched together to make grain maps. A CL detector was inserted to take CL images of individual grains. These same grains were elementally mapped by using an EDS detector.

Results

Bulk-Rock Geochemistry

The silica composition of pumices and lavas within the Roseau Valley range from 56-66 wt. %, indicating they are andesites and dacites (Figure 11). The deposits from these locations have been dated (Figure 4), allowing for analysis of stratigraphic trends. The SiO_2 content in the samples tends to be higher in the older samples, and lower in the younger samples (Figure 11). Deposits in the Goodwill Quarry were dated using U-Th/He of zircons to as old as 55 ka (Howe et al., 2014) and have a silica content ranging from 62-65 wt. %, with one outlier at 57.8 wt. %. Samples from the Casso estate have been dated using U-Th of zircon rims to as young as 6 ka (Babiak, 2016). The silica content in these samples range from 58-59 wt. % SiO_2. These two sample locations are exemplary of the trend in the data, as the other samples plot at intermediate ages and silica contents. The stratigraphic trend shows the younger samples are generally less evolved.

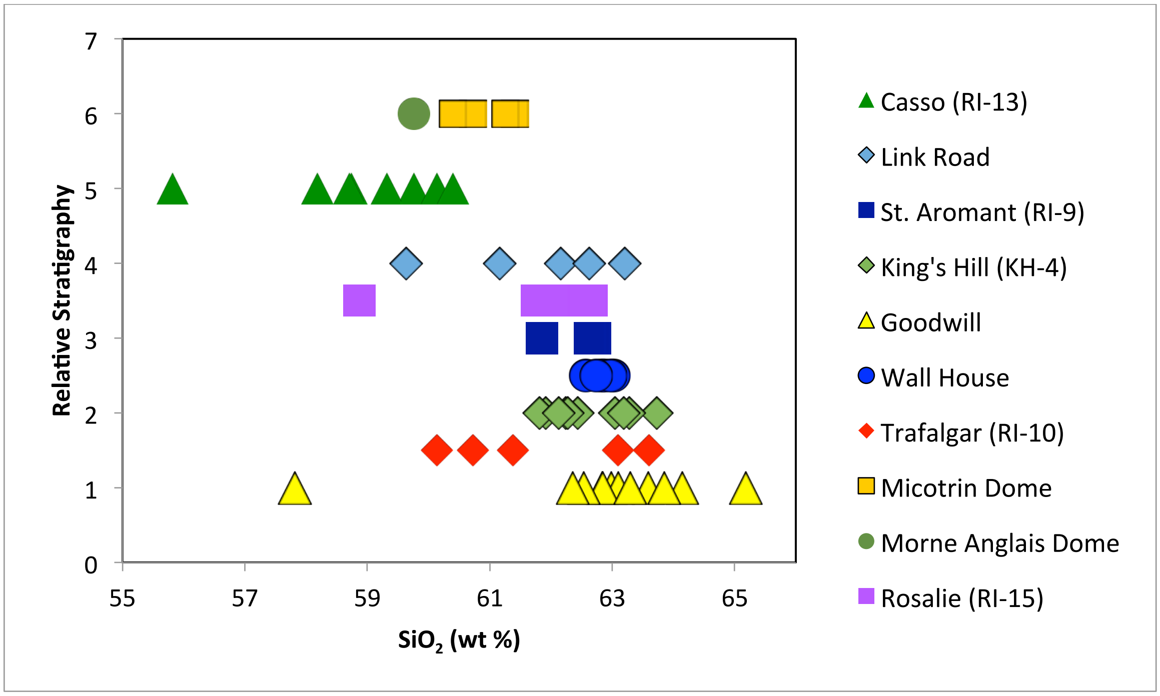

Figure 11. The silica content of samples in the Roseau Valley and Rosalie are plotted against their relative ages, with 0 as the oldest and 7 as the youngest based on U-Th zircon rim ages (Frey et. al, 2016). These distributions show that the younger samples are typically less evolved than the older samples.

The major element composition of Fe_2O_3 ranges from 5-9 wt. %, CaO ranges from 4-7 wt. %, TiO ranges from 0.4-0.7 wt. %, MnO from ranges 0.12-0.22 wt. %, Al_2O_3 ranges from 15.5-19 wt. %, and MgO ranges from 1.5-3.5 wt. %. The major element chemistry is variable for different pumice clasts in the Roseau Valley. Samples from the same location generally plot in clusters, however all of the locations vary within 2-4 wt. % SiO_2, with a few lesser-evolved outliers in the Goodwill and Rosalie samples. The Wall House samples are very tightly constrained in composition and vary by only 0.4 wt.% SiO_2.

Many of the oxides follow a linear trend, showing their relationship to silica content and magmatic evolution. Fe_2O_3, CaO, and MgO decline with increasingly evolved compositions. Al_2O_3 shows a less pronounced trend, however in general show a decline in concentration with evolution. Na_2O also shows a roughly decreasing trend with evolution, however its content in the Casso samples varies independently of silica content. Some elements and oxides increase with evolution, for example K_2O clearly displays a positive linear relationship with silica content. K_2O also separates the samples into two fields around 1.2 wt.%, and 1.6 wt.%. Morne Anglais had a much lower K_2O content than the rest of the samples, at 0.7 wt.% compared to the rest of the samples at 1.1-1.8 wt.%. Some trends are also visible in trace elements. The composition of Sr ranges 180-240 ppm and Ba ranges 150-300 ppm. Ba increases with silica content, whereas Sr varies independently within each location and has no increasing or decreasing trend with SiO_2 (Figure 12, 13).

Certain sample locations are distinctive in their major and minor element compositions. For example, Casso (RI-13) is not only less evolved than most of the samples, but varies in composition much more than other samples which cluster closer together. For Al_2O_3 and CaO, Casso samples vary by ~2.5 wt.%, whereas the other samples generally vary by 1-0.5 wt.% (Figure 12). Casso samples also vary more than other samples in Na_2O (spanning ~1.3 wt.%) and in trace elements; Sr (spanning 50 ppm) and Ba (spanning 100 ppm) (Figure 13).

The samples from Rosalie (RI-15) are located on the east coast and not within the Roseau Valley and have been previously grouped with the Roseau Ignimbrites due to proximity and broadly similar chemistry and mineralogy compared to Roseau deposits (Smith et al., 2103). The RI-15 samples are typically clustered together, except for one less evolved outlier. These samples also usually plot closely with other samples such as St. Aromant (KH-4) and Wall House in most of the major oxides; Al_2O_3, CaO, Fe_2O_3, MgO, and Na_2O. However, in K_2O, Rosalie samples plot distinctively higher than the others, shown by the pink circle (Figure 12). Rosalie and St. Aromant again overlap in their Sr composition and plot lower at 203-211 ppm Sr, whereas Wall House is more variable at 198-215 ppm Sr. Rosalie and St. Aromant also overlap in their Ba composition at 235-260 ppm Ba, but Wall house plots tightly clustered at a lower ppm of 225-345 ppm Ba. Overall, Rosalie and St. Aromant display little compositional difference in bulk rock chemistry besides in K_2O, whereas Wall House is more distinctive.

Samples from Trafalgar (RI-10) and King's Hill (KH-4) are less clustered, as they span a greater silica content than the other samples, but there are also more numerous samples. The fields of these two locations typically slightly overlap, as Trafalgar spans a greater range in SiO_2 content of ~60-64 wt.% and King's Hill spans ~62-64 wt.%. Kings Hill also overlaps with Rosalie, Wall House, St. Aromant, and the Goodwill samples. Na_2O separates some of these fields, and Kings Hill plots at 3.1-3.3 wt.%, lower than St. Aromant and Goodwill at 3.3-3.6 wt.%. For Kings Hill's Sr composition, the samples only overlap with Goodwill. Sr separates these locations the best compared to the other plots, as Rosalie and St. Aromant plot at 203-211 ppm, lower than King's Hill, Trafalgar and Goodwill, which contain 228-208 ppm Sr (Figure 13).

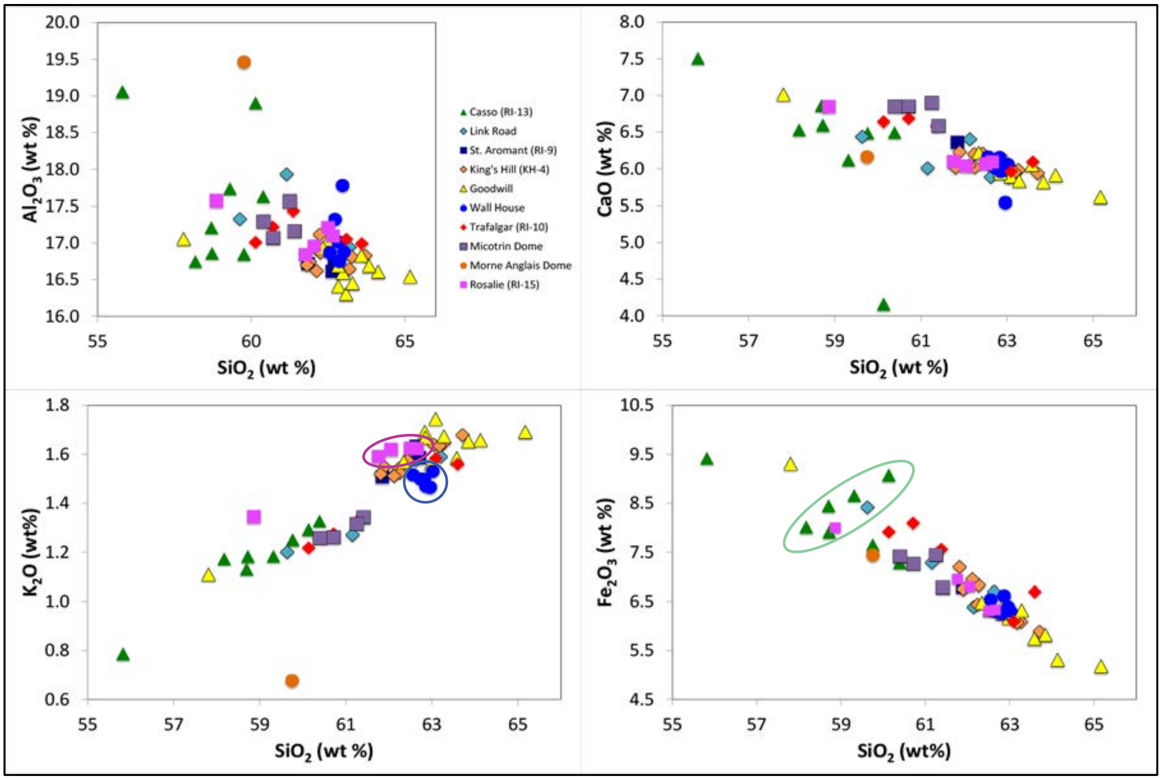

Figure 12 Bulk rock chemistry compositions of major oxides, Al_2O_3, CaO, K_2O, and Fe_2O_3 vs. SiO_2, from powdered pumice and lava samples from the Roseau Valley and Rosalie. Relevant and distinctive fields are circled and colored corresponding to the location they represent. A major trend is that the Casso samples (green) are much more variable than the other sample locations.

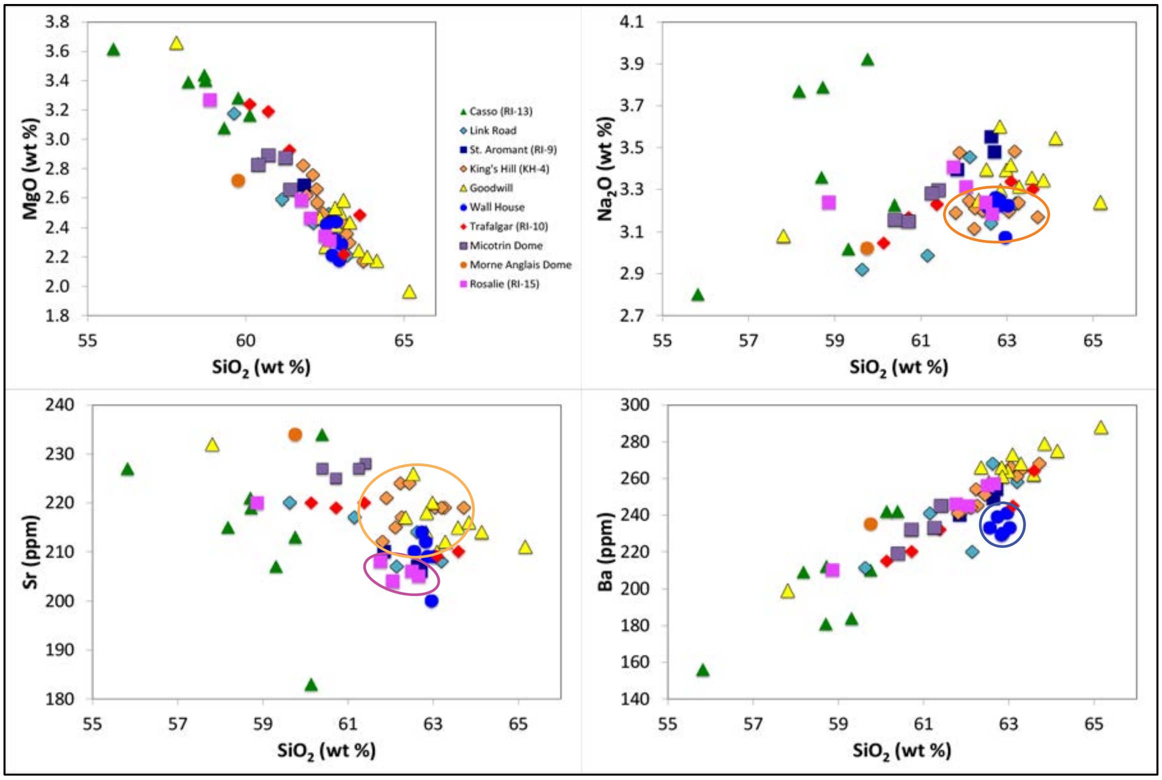

Figure 13. Bulk rock chemistry compositions of major oxides, MgO Na_2O, and trace elements Sr and Ba vs. SiO_2, from powdered pumice and lava samples from the Roseau Valley and Rosalie. Sr separates the samples out the best, with Rosalie and St. Aromant plotting at low concentrations, and Kings Hill separated from all samples but Goodwill.

All the samples in the Roseau Valley typically follow a parallel signature in their REE (rare earth element) compositions. The samples are enriched in the LREE, more depleted in MREE, and slightly enriched in HREE. There is a concave MREE to HREE trend (Figure 14). The LREE to HREE ratio is approximately 3 to 1. However, Casso (RI-13) samples are all more enriched in MREE and LREE than the rest of the Roseau samples and peak sharply at Eu. Based on major and trace elements, Casso has the most variable and distinctive bulk rock chemistry.

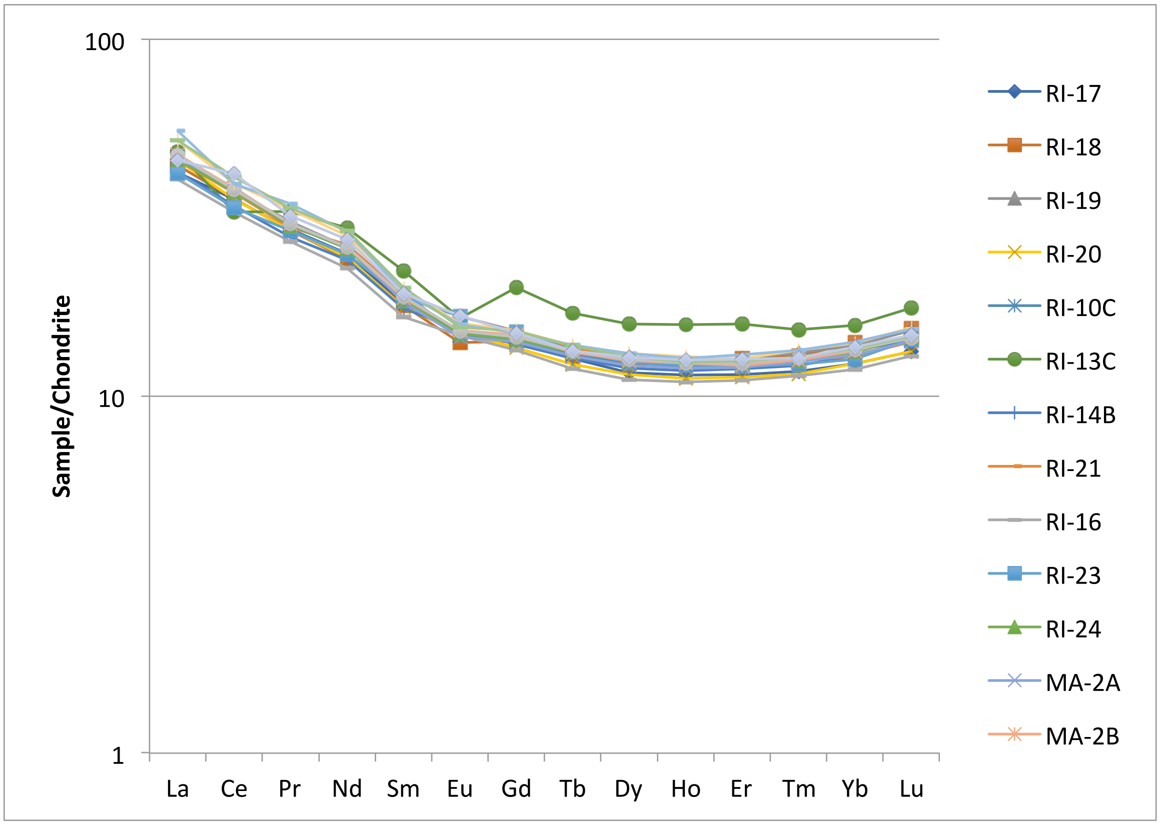

Figure 14. The rare earth elements from bulk rock chemistry exhibits and typical arc-volcanic signature. The samples are enriched in LREE and depleted in MREE, and there is a concave relationship between MREE and HREE. RI-13 has a different rare earth signature than the other samples, and is more enriched in the MREE and HREE.

Cathodoluminescence Zoning

Grain mounts of samples RI-9, RI-10, RI-15, RI-13, and KH-4 were analyzed on the Scanning Electron Microscope (SEM). None of the samples were zoned using backscatter electron detection (BSE). Cathodoluminencence (CL) zoning, however, was detected in all grains. The CL zoning of grains were grouped into 5 categories: oscillatory, bright core, bright rim, irregular core, dark core, and radial/streaky (Table 1).

Table 1. Percentages of zoning textures of apatite crystals.

Sample #	N	Oscillatory %	Bright core %	Bright rim %	Irregular Core %	Dark Core %	Radial or Streaky %
RI-13	52	75.0	23.1	36.5	11.5	9.6	0
RI-15	56	92.9	39.3	5.4	32.1	12.5	0
KH-4	37	97.3	18.9	10.8	5.4	29.7	0
RI-10	17	11.8	0.0	35.3	0.0	88.2	76.5
RI-9	7	0	0	0	0	25.0	100.0

Oscillatory zoning refers to regular changes in the crystal composition that develop as the crystal grows under changing conditions. This zoning was very common in all of the samples except RI-10 and RI-9. However, RI-10 and RI-9 are the only grains to have the radial and streaky zoning signature. In the few grains of RI-10 that showed oscillatory zoning, the streaky pattern seemed to overlay an oscillatory pattern (Figure 15 A) In RI-10 and RI-9, the radial zoning is visible when looking down the c-axis, best described as bright dendritic streaks radiating from the core to the rim. When looking along the c-axis, the streaks are parallel to the c-axis and fade out in the dark cores of some grains (Figure 15 A, B).

The sample locations all have characteristic distributions of bright cores, bright rims and dark cores. There does not seem to be a correlation between these traits within samples. For example, RI-13 has 36% bright rims and 9% dark cores, whereas RI-15 has 5% bright rims and 13% dark cores. This shows that having more bright rims do not correlate with having more dark cores. KH-4 has 10% bright rims, but the highest amount of dark cores at 30%. This shows that there are no shared dark-to-bright core to rim patterns repeated throughout sample locations, and the locations have unique textural patterns.

Comparison across sample locations shows some striking differences in their zoning characteristics. RI-9 and RI-10 are the only samples to have the any streaky or radial zoning, at 76% and 100% respectively. However, RI-10 has 88% dark cores, whereas RI-9 only has 25%. The dark cores in RI-10 may not appear the same as the other samples, due to the bright streaky and radial zoning near the rims of the grains. The brightness from this secondary zoning pattern may make the cores appear relatively darker. The resolution of the RI-9 images is low, and only 7 grains were imaged, compared to 17 in RI-10, which may contribute to their differences. Neither of these samples contain irregular cores, which are present in all the other samples.

32% of grains in RI-15 have irregular cores, over twice as many as the other samples. RI-15 also has the highest amount of bright cores, at 39%. RI-13 contains 11% irregular cores, but has the highest amount of bright rims, at 36%. KH-4 has only 5% irregular cores, but has 30% dark cores, much higher than both RI-13 and RI-15. One more important observation is that the irregular cores in RI-13, RI-15, and KH-4 are bright cores. There are no discernable irregular dark cores, and the bright irregular cores are usually homogenous in their CL brightness and are not zoned.

The zoning characteristics of every sample are unique. The major observations to be made from the CL images are:

1) Each sample has unique apatite textural distributions.
2) A radial and streaky zoning pattern is only seen in RI-9 and RI-10 and in some grains overlays a primary, oscillatory zoning pattern.
3) Bright irregular cores are observed only in RI-13, RI-15, and KH-4 at varying amounts.
4) 30% of grains in KH-4 have dark cores.

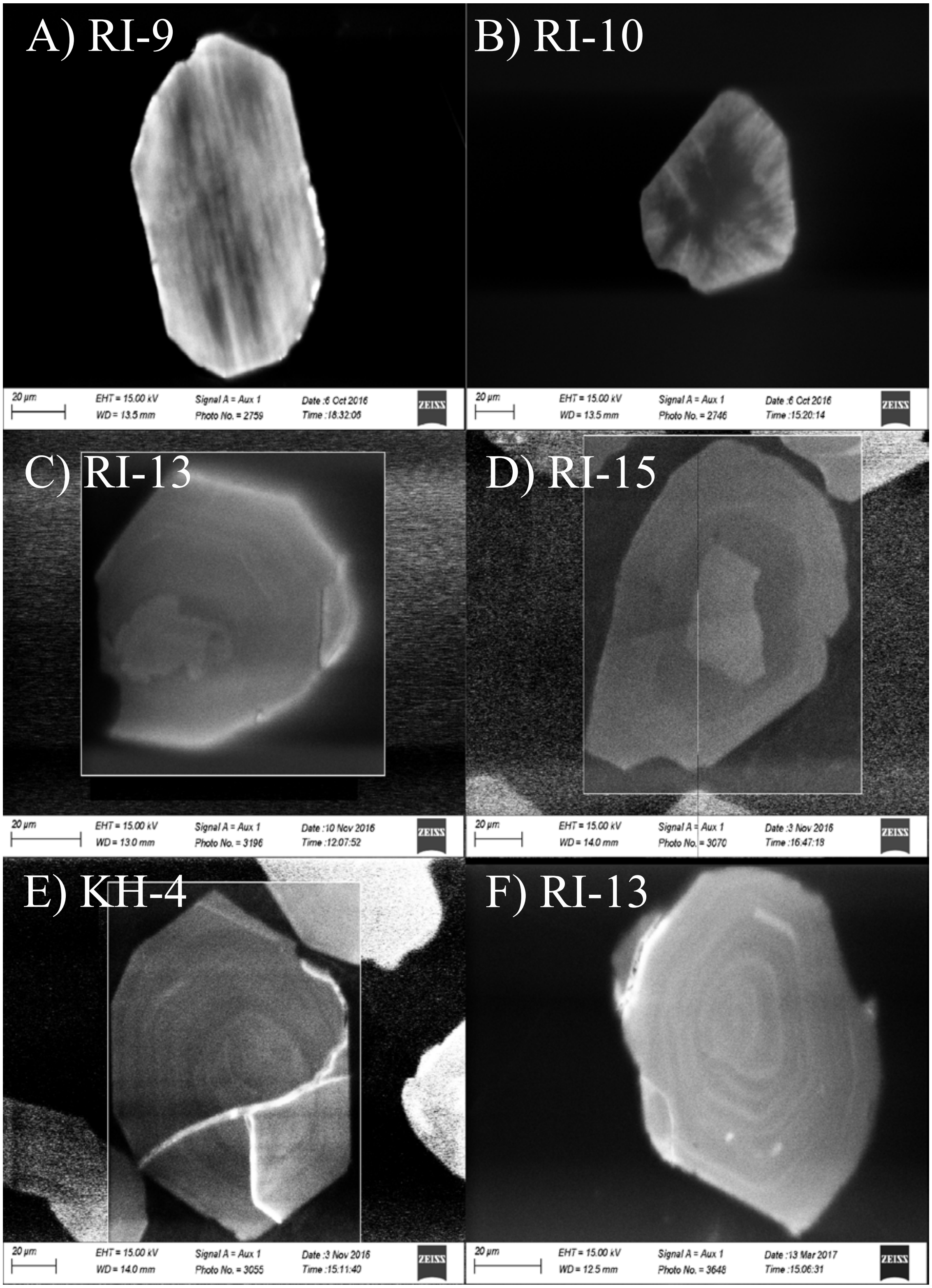

Figure 15. Cathodoluminescence images of apatite. A) And B) exhibit radial and streaky zoning, C) and D) are examples of irregular cores, and E) and F) are examples of oscillatory zoning.

Elemental Mapping

Elemental maps of Cl, F, Si, S, Ti, P, Na, O, K, Fe, Ca, and Al were created for grains in samples KH-4, RI-15, RI-13, RI-9, and RI-10. Samples RI-15, RI-13, and KH-4 show no elemental zoning in over 20 grains imaged. RI-9 and RI-10 are zoned in chlorine and fluorine in almost every grain imaged (Table 2). The grains were not zoned in any other elements (S for example) than Cl and F (Figure 16). The main type of elemental zoning observed is a core to rim change in the crystals. The cores are typically enriched in chlorine, and the rims were gradationally enriched in fluorine. The cores of larger grains are homogenously chlorine enriched, and near the rim (at ~20 μm) starts a gradational change into fluorine enriched and chlorine-depleted rims (Figure 17).

Another zoning texture observed is a “streaky” signature, similar to the CL zoning in RI- and RI-10 (Figure 18). In RI-10, ~80% of grains were zoned from the core to rim in chlorine and fluorine, and 38% of grains had streaky zoning in chlorine and fluorine. In RI-9, 96% of grains were zoned from the core to rim in chlorine and fluorine, and 52% of grains had streaky zoning in chlorine and fluorine (Table 2).

Table 2. Chlorine and Fluorine zoning percentages.

Sample #	N	Cl Core and F Rim Zoning %	Cl and F Streaky Zoning %
RI-13	8	0	0
RI-15	17	0	0
KH-4	4	0	0
RI-10	16	81.25	37.5
RI-9	25	96	52

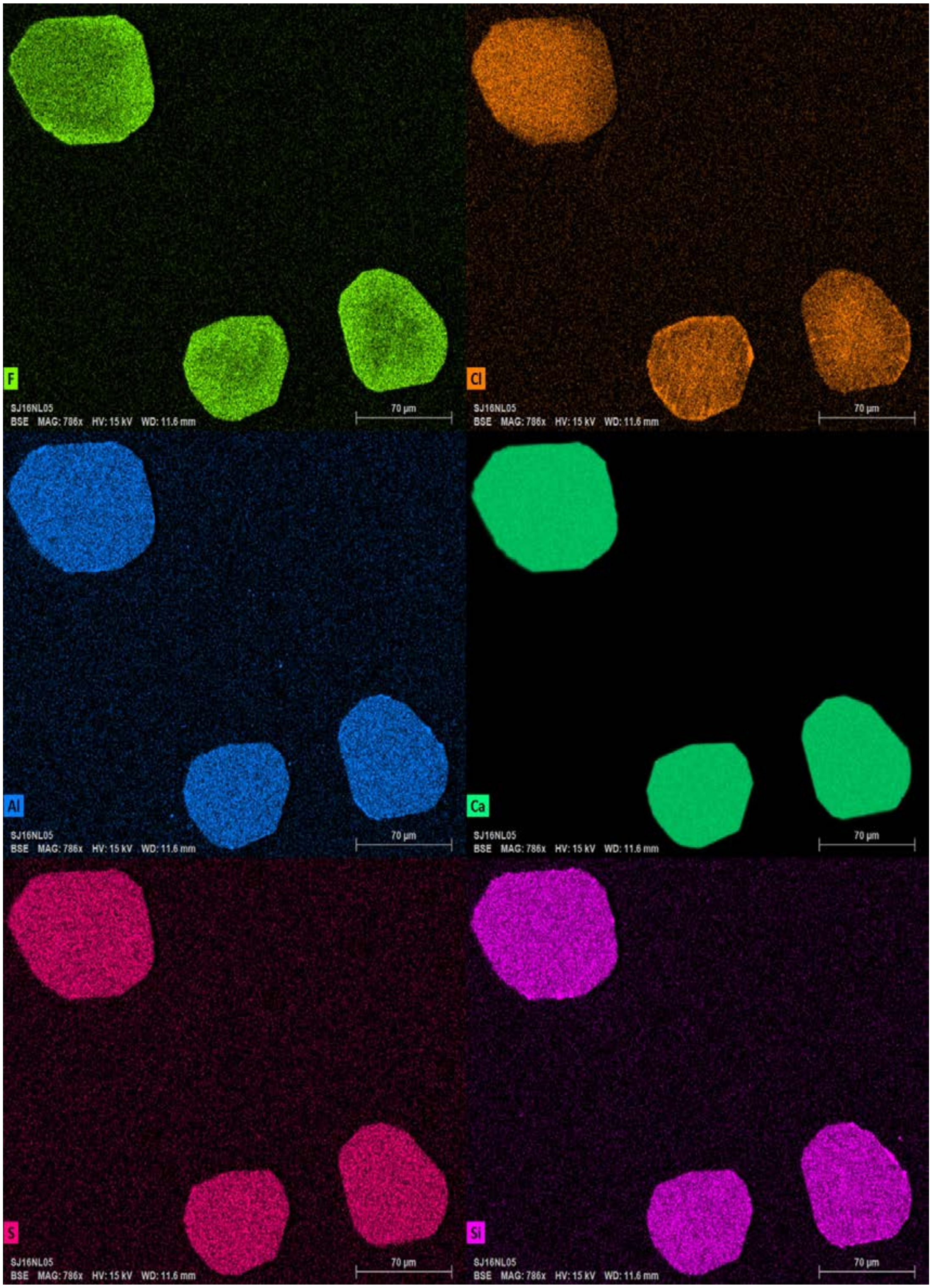

Figure 16. Elemental zoning RI-9. These elemental maps are representative of the typical chorine and fluorine zoning in apatite grains from this sample, but the absence of any other elemental zoning such as aluminum, calcium, sulfur (another volatile element), and silica.

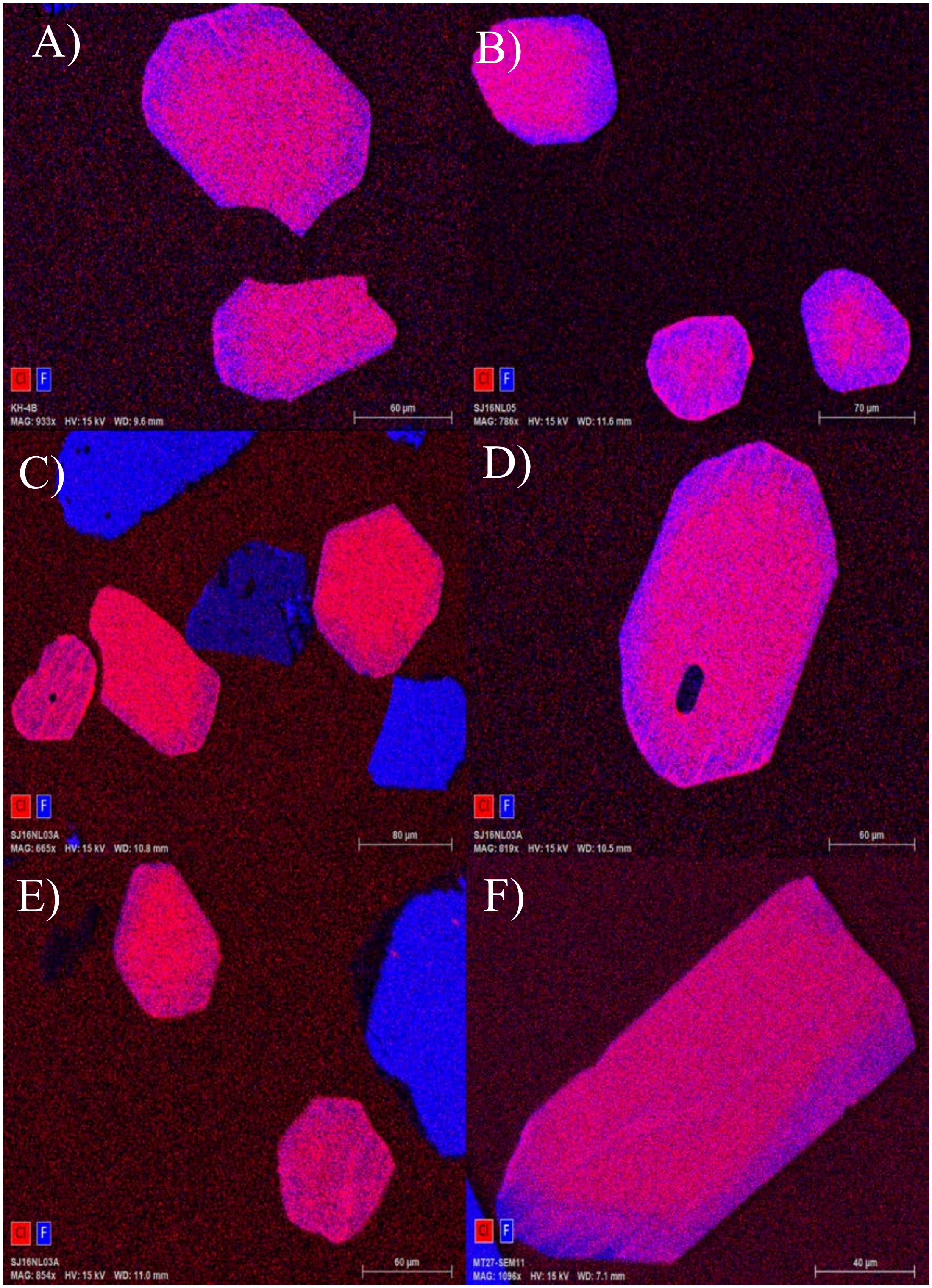

Figure 17. A)-F) show examples of chlorine and fluorine zoning in the RI-9 sample. Most of the cores are enriched in chlorine, and usually these cores grade into fluorine enriched rims. Some of these samples have a streaky pattern in the rim of the crystals. C) The grain to the far left is an example of a grain which has streaky zoning, but no core to rim zoning, showing that these two zoning patterns do not always occur together.

Correlation of CL to elemental zoning

The cathodoluminescence was compared to the elemental zoning maps of grains to look for any similarities. It was not expected that the CL would correlate to chlorine or fluorine, since these elements are not CL activators. A study by Roeder et al. (1987) found that bright CL in apatite is due to rare or trace elements which substitute into the apatite crystal structure, such as Mn^{2+}, Sm^{3+}, Dy^{3+}, Tb^{3+}, Eu^{2+}, and Eu^{3+}, which could not be detected by elemental mapping. However, these elements could be associated with the partitioning of other elements into the apatite structure.

A comparison of the CL maps and elemental maps shows that the CL oscillatory zoning is not shown elementally. Grains A-B (Figure 15) shows oscillatory zoning near the rim in CL, however there is no such sharp change in chlorine or fluorine in the elemental map. The core of the grain is dark in CL and this same area is enriched in chlorine. However, the lower grain in the C-D map has a weakly bright core in CL, and also has a slightly chlorine enriched core, which shows that CL brightness does not correlate with chlorine content for core to rim zoning.

The streaky elemental zoning may be related to the streaky CL zoning. In some images, bright streaks of CL also occur in the elemental map of the same grain as streaks of enriched chlorine in the fluorine rims (Figure 18). Certain defined streaks and radial zones of enriched chlorine can be correlated to bright streaks in CL, shown by the white lines in figure 17. Some of the other streaks in the grains are not observed in the elemental maps, showing this may be a weak correlation. Overall, the CL maps do not correlate to the elemental maps except for some of the most prominent streaky and radial CL signatures, which appear as chlorine enriched zones.

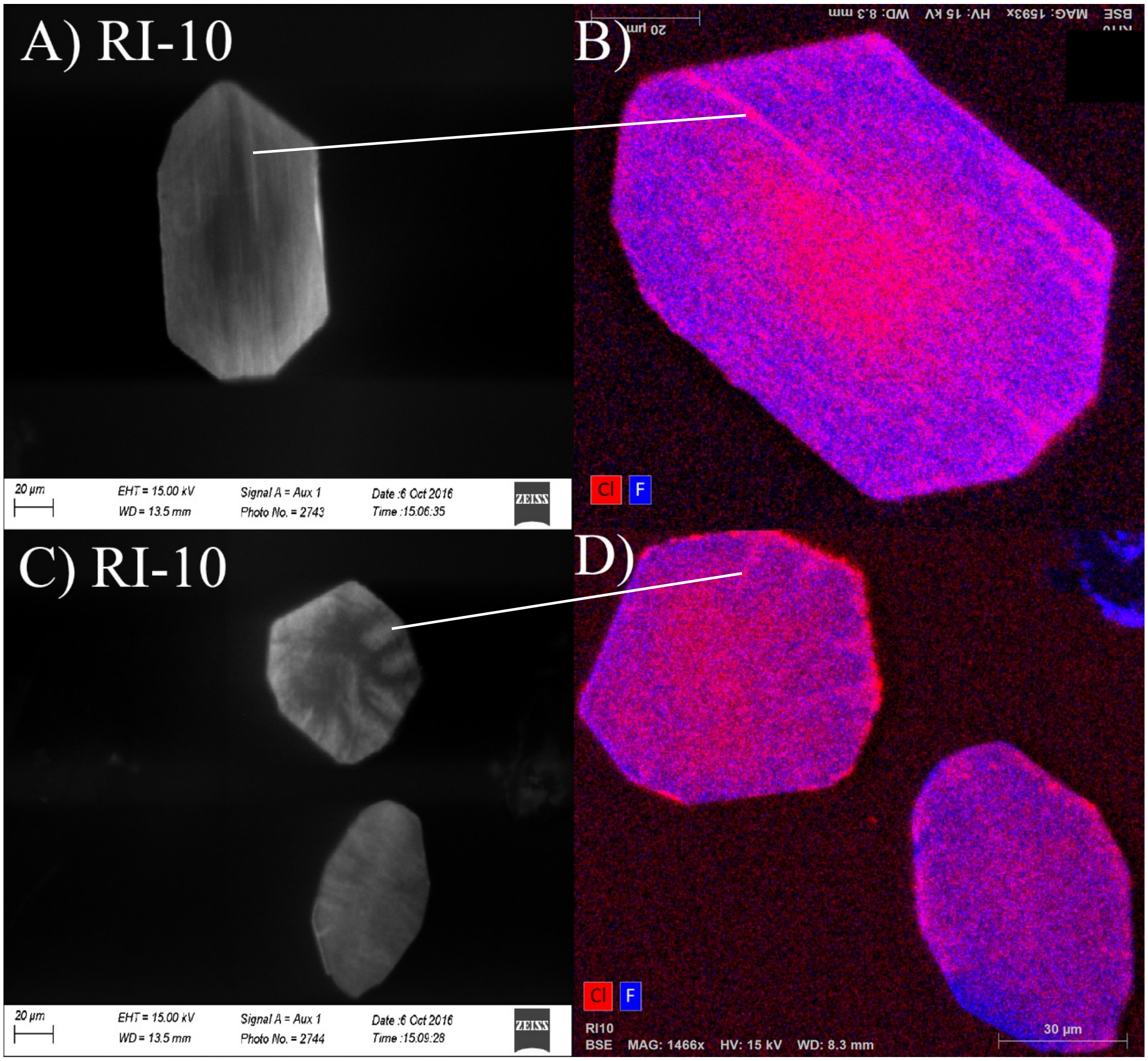

Figure 18. These images from RI-10 show the relationship between the CL zoning and the elemental zoning of chlorine and fluorine. A) shows a grain with oscillatory zoning as well as streaky zoning. B) shows an elemental map of the same grain. The chlorine and fluorine zoning does not show the same sharp, oscillatory zoning in A, but has similar streaky zoning. C) shows a CL map of two other grains, both with radial zoning and one with a brighter core. D) shows that again the radial zoning may be related to the bright streaks of chlorine.

Single Apatite Grain Chemistry

The single apatite chemistry from laser ablation provides more ways to distinguish samples RI-10, RI-9, RI-15, RI-13, and KH-4. Certain ratios of rare earth elements show that the samples have distinctive chemistries, and the ratios represent

LREE/HREE ratios. Plots of Sr/Y vs. Ce/Lu and La/Nd vs. Sm/Dy illuminated distinct chemical signatures (Figure 19, 20).

In the plot of Sr/Y vs. Ce/Lu, there are some striking differences between the samples. RI-10 grains are tightly constrained at an intermediate Sr/Y composition of 0.33-0.35, whereas the other samples spanned greater ranges. RI-9 samples plotted similarly to RI-10, but spanned a wider compositional range of 0.27-0.48 in Sr/Y. Both RI-9 and RI-10 overlap with the fields of RI-13 and RI-15.

In both plots, KH-4 spans higher values than any of the other samples. In Sr/Y, KH-4 grains spanned compositions from 0.31-0.61, in Ce/Lu they plotted from 172-310, in La/Nd they plotted 0.58-0.74, and in Sm/Dy they spanned 1.3-1.6. In La/Nd and Sm/Dy KH-4 almost completely is separated from the rest of the samples (Figure 20). KH-4's field overlaps with a few of the highest ratios in RI-9 and RI-15. These plots show that KH-4 apatites have a distinctive chemistry compared to the rest of the samples.

The RI-15 samples span almost as large a field as KH-4 in Sr/Y, from 0.27-0.51. This sample was separated into grains with irregular cores, and grains with regular cores. The irregular core samples generally plotted lower in all ratios, however still overlap with a significant proportion of regular core grains. In Sr/Y, the irregular cores plotted from 0.27-0.4, and the regular cores plotted from 0.27-0.52. In La/Nd, none of the irregular core grains overlapped with the KH-4 field, but in Ce/Lu their fields slightly overlap. The RI-15 field also overlaps with the RI-13 samples.

The grains from sample RI-13 plotted at the lowest values of Sr/Y at 0.23-0.38 and Ce/Lu clustered mostly around 122-152. This sample also had irregular cores in CL, and these grains were plotted separately. The irregular core grains plotted from 0.25-0.3

in Sr/Y. This is a similar pattern to the irregular cores in RI-15, which plotted at a lower range that the regular core samples, but still generally overlapped. This shows that the irregular cores of RI-13 and RI-15 plot slightly differently than the samples as a whole. It is important to note that the entire grain was ablated on the ICP-MS, not just the irregular cores of grains.

KH-4 contains 30% dark cores, more than RI-13 and RI-15, which have 9-12% dark cores. RI-13 plotted the lowest in Sr/Y and Ce/Lu. RI-15 spanned a larger range than RI-13 but still plotted lower than KH-4 in all ratios. The irregular, bright cores plotted slightly lower in Sr/Y than the rest of the samples. This may indicate that there is a correlation between higher LREE/HREE values in KH-4 and dark cores, compared to the low LREE/HREE values in RI-15 and RI-13 with brighter cores.

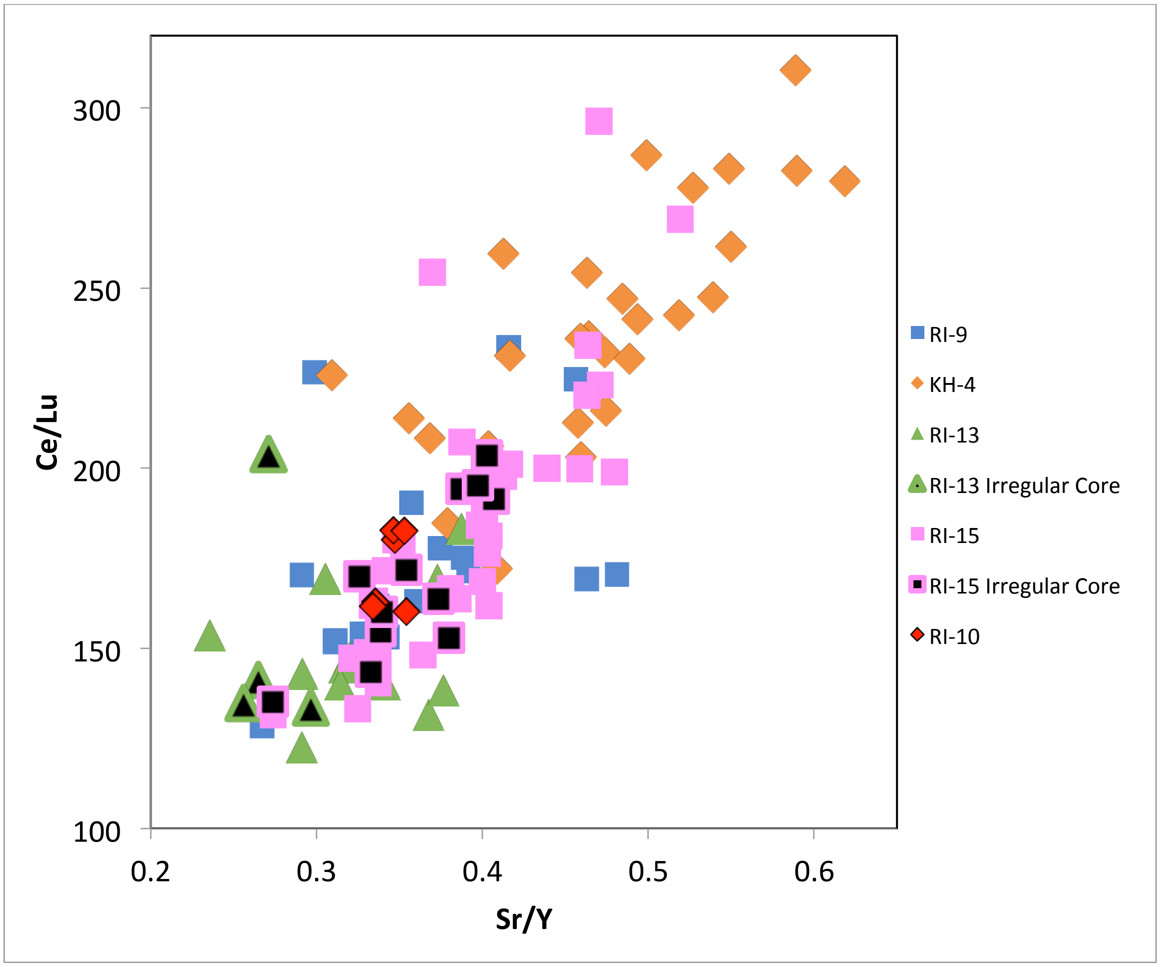

Figure 19. Sr/Y vs. Ce/Lu of single apatite grains. KH-4 plots at distinctively higher values than the other samples. RI-9 plots at intermediate values, overlapping with every other sample. RI-10 plots at a distinct Sr/Y value, which also overlaps with the fields of almost every sample but KH-4. The grains in RI-15 and RI-13 with irregular cores are plotted as the same color as the whole sample but with black centers. The irregular cores plot at slightly lower ranges in both Sr/Y and Ce/Lu than the samples as a whole. RI-13 plots at lower values than the rest of the samples, but still significantly overlaps with RI-15, which spans almost all Sr/Y values of all the samples.

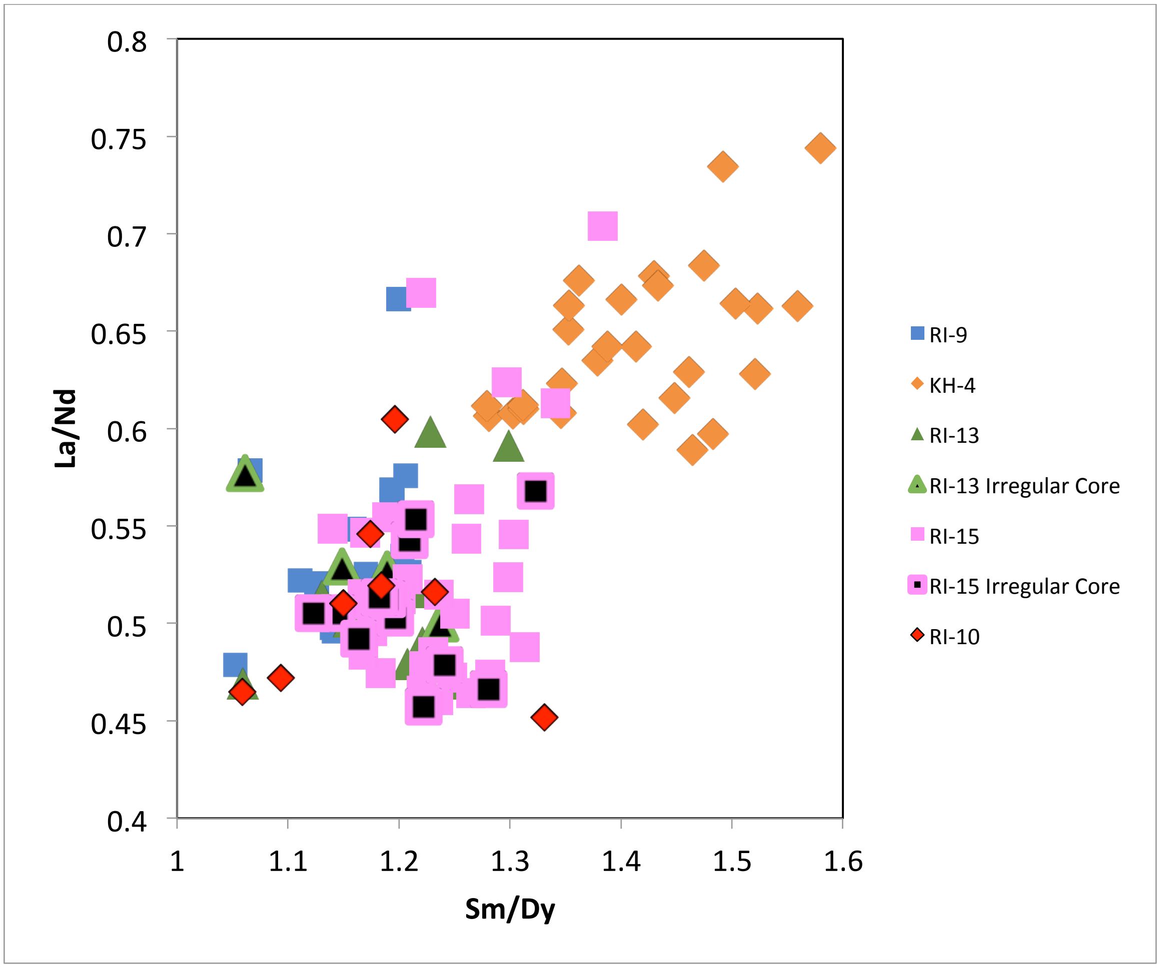

Figure 20. This plot of La/Nd vs. Sm/Dy of single apatite grains shows that KH-4 is compositionally different and plots at higher values than the rest of the samples. RI-13 no longer plots the lowest but overlaps with the other samples. This plot is different from Figure 19 in that KH-4 looks even more distinct, while the other samples plot closer together.

Comparison of Whole-Rock and Apatite Chemistry

The apatite chemistry of KH-4 was much more distinctive than its whole rock chemistry. In the major and minor elements besides Na_2O, KH-4's field overlaps significantly with RI-15, RI-9, and RI-10 and has similar silica content (Figure 12, 13). However, in the apatite rare-earth element ratios, KH-4 plots higher than these other samples with only slight overlap with RI-9 and RI-15, and not at all with RI-10. This shows that there are distinctions in apatite chemistry that cannot be seen in whole rock chemistry. RI-13 also plots differently in the single apatite chemistry than the whole rock samples. For whole rock oxide composition, RI-13 spanned much larger compositional ranges than the other samples, however in single apatite chemistry the compositional field was no larger than other samples. Another difference is in whole rock major and trace elements, RI-13 did not overlap with RI-15 at all, except for one outlier. However in the apatite chemistry, their fields mostly overlap. RI-13 also overlaps with RI-9 and RI-10 in single apatite grain chemistry, however it is much less evolved and does not look similar to these samples in whole rock chemistry.

Studies have shown that the relationship between host rock and apatite REE and Sr content can trace petrogenetic processes. REE content and Sr content of apatite vary systematically with rock type and silica content, and also is affected by other REE bearing phases like plagioclase. Inconsistencies between apatite and host rock chemistry may also indicate magma mixing or heterogeneity in their parent melts (Chu et al., 2009). We were able to plot the host-rock Sr content to that of the apatites. The apatite Sr composition shows no linear relationship to the WR silica content (Figure 21). RI-13, the least evolved sample, has the largest and highest range of Sr content at 278-457 ppm. RI-15 and KH-4 have similar ranges at 307-447 ppm and 358-441 ppm, respectably. RI-10 and RI-9 are both lower in apatite Sr than the other samples. RI-10 ranges from 322-399 ppm with one outlier at 201 ppm. RI-9 ranges from 350-394 ppm with one outlier at 278 ppm.

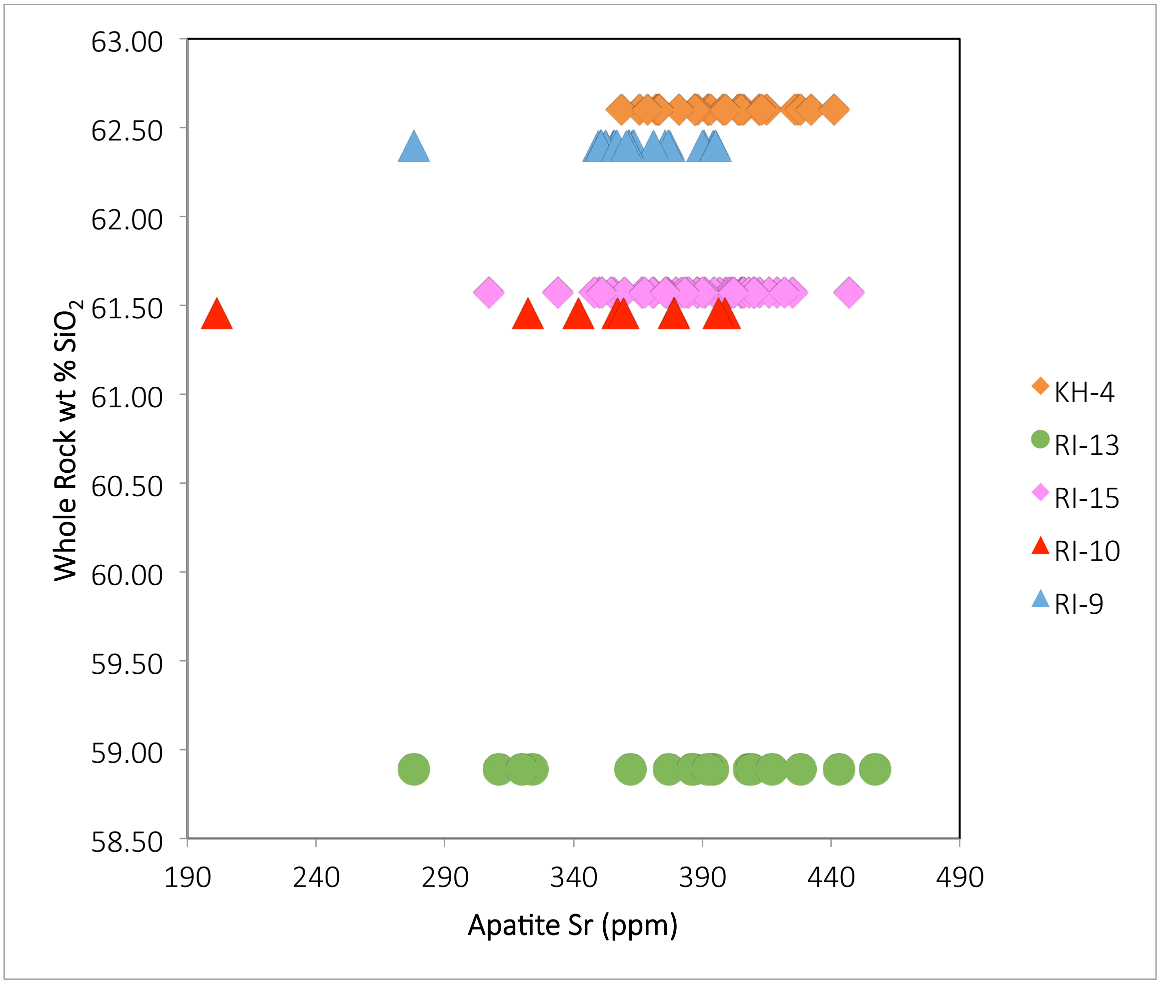

Figure 21. Average whole rock SiO_2 wt. % plotted with individual apatite grain Sr composition. The data shows that there is no clear linear trend between Sr in apatite and evolution.

A comparison of the WR Sr composition and the apatite Sr composition also shows that the Sr composition of the host rock has no linear correlation to the Sr content of the apatite grains (Figure 22). A line with a 1:1 relationship to the apatite and whole rock shows that the apatites have consistently higher Sr ppm that their host rocks. It also shows that there is not a correlation between silica content and host rock Sr content. RI-13, the least evolved sample, plots higher than RI-15 and RI-9 for WR Sr content.

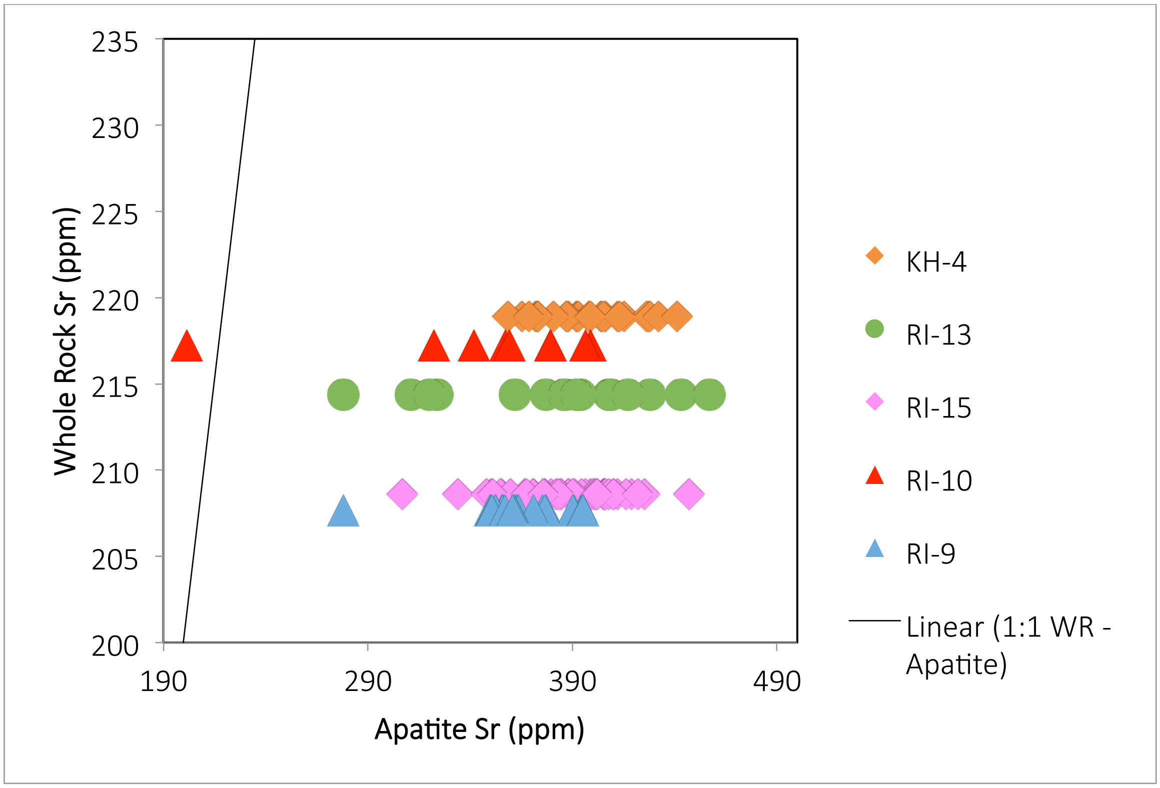

Figure 22. Whole rock Sr content vs. Apatite Sr content. The apatites consistently have higher Sr than their host rocks, with no linear correlation between their compositions.

Comparison of Apatite Chemistry with Chronology

There does not appear to be any correlation with apatite LREE/HREE ratios and stratigraphy. KH-4 has the highest Yb/Dy ratio and is one of the older deposits. RI-10, the oldest deposit has a similar Yb/Dy ratio to the youngest deposit, RI-13. This shows that there is no progression of apatite composition with age.

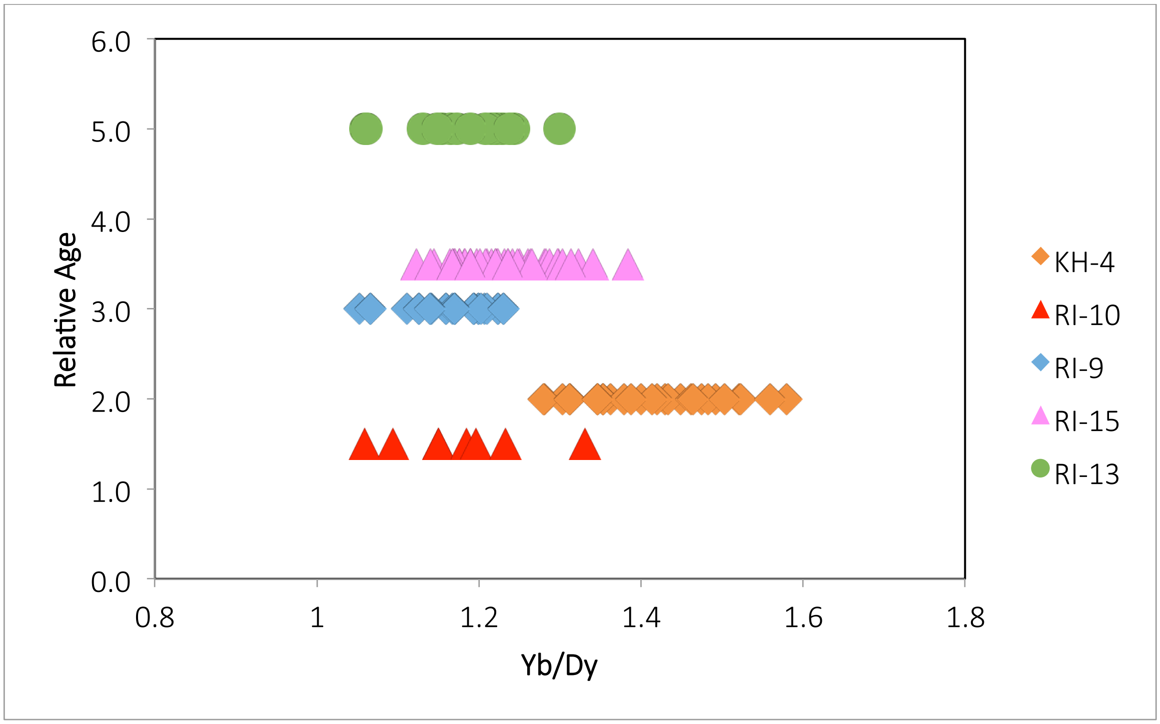

Figure 23. The relative age of the eruptive deposits and their Yb/Dy content. There is no linear relationship between these factors.

Oxygen Fugacity

An analysis of Fe-Ti oxides for temperature was done by Frey et al. (2016), based on the thermometer developed by Ghiorso and Evans (2008). The compositions of co-existing oxides are also sensitive to redox state, so calculations yield not only temperature, but also oxygen fugacity of fO_2. The resulting oxygen fugacity values relative to the nickel-nickel oxide buffer (NNO) shows that certain deposits have distinctive values (Table 3). KH-4 has a strikingly high value at 0.86, while the rest of the Roseau samples plot from 0.37-0.35. The Grand Bay ignimbrite samples show even lower values at 0.35-0.28.

Table 3. Oxygen fugacity values for southern Dominica samples.

Sample	fO_2 (ΔNNO)
KH-4	0.86
RI-13	0.37
RI-15	0.37

RI-9	0.35
GB-12	0.28
GB-10	0.15

DISCUSSION

The Single-Source Hypothesis

Previous island-wide studies of Dominica have proposed that one large magma chamber supplies magma to the volcanic centers, with the exception of Morne Aux Diables in the north (Lindsay et al., 2005; Smith et al., 2013; Howe et al., 2015). Lindsay et al. (2005) proposed that there is geochemically homogenous andesitic source magma for the southern volcanic centers, and geochemical variations are due to the degree of differentiation prior to eruption. Island-wide similarities in the petrology of erupted deposits led Smith et al. (2013) to propose that most of the volcanic centers are connected at depth. A model was presented in which smaller plutons amalgamated through small magma additions beneath the island to produce an island-wide batholith, a model which has been used to explain continental batholith intrusions (Glazner et al., 2004). The small magma batches accumulated, eventually forming a batholith, whose homogenous nature was sustained by convection and continuous inputs of new magma (Annen, 2011). Howe et al. (2014) added to this hypothesis when studying the Roseau Ignimbrite. Using U-Th/He ages and the presence of paleosols, they found that the Roseau ignimbrite was composed of up to 7 homogenous eruptive events, disproving a one-eruption hypothesis proposed by Sigurdsson and Carey (1980). However, Howe et al. (2014) focused on whole rock chemistry, glass chemistry, and the chemistry of abundant minerals, and did not investigate apatite chemistry.

Howe et al. (2015) also used U/Th zircon ages to link the volcanic centers. They found volcanic centers up to 40 km apart contained overlapping age populations. While there was heterogeneity in the zircon rim ages, suggesting some zones may be crystallizing independently, they found each volcanic center had distinctive zircon probability plots and suggested an overall north to south migration of effusive volcanism. Some volcanic centers yielded similar zircon populations, indicating simultaneous magmatic activity beneath these centers, and potential horizontal connectivity.

Couch et al. (2001) proposed that a large, convecting magma body exists beneath Montserrat. They proposed that convective mixing in a magma chamber could cause disequilibrium features such as reversely zoned crystals, resorbtion features, and varying mineral compositions. Magma mixing, or the injection of basalt into andesite could also cause disequilibrium features, but they argued magma mixing could not have caused the amphibole crystals in mafic inclusions they observed. Smith et al. (2013) thus attributed the subtle chemical and textural variation between different deposits from individual centers to the island-wide convection of a batholith.

Smith’s model was also used to explain the eruptive style on Dominica. The two large calderas on the island; Wotten Waven and Morne Trois Piton were caused by Plinian-style eruptions (Hughes and Mahood, 2008), and were followed by Peléan-style dome forming eruptions and block and ash flows. Smith et al. (2013) proposes that there were basaltic injections into a large andesitic crystal mush beneath Dominica, which caused magma to rise to the top of the chamber. This injection and re-melting produced volatiles leading to Plinian caldera-forming eruptions and pumiceous deposits. Then, later eruptions tapped lower, volatile depleted magma leading to Peléan type activity. Smith et al. (2013) also identified the 6 “seismothermal zones” where there are shallow earthquakes, geothermal fields and phreatic explosions. They suggested that these zones represent the "active batholith" beneath where mafic injections into the batholith remobilize melts by convection and come to the surface in areas of unstable crust.

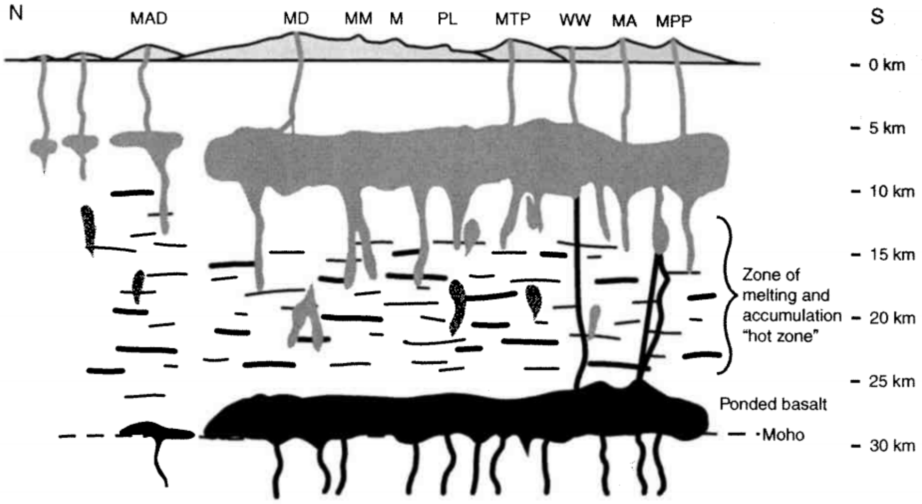

Figure 24. Smith model. The proposed single batholith model from Smith et al. (2013). The model involves a horizontally homogeneous magma body beneath the island.

Apatite Chemistry and Magmatic Processes

The research presented in this study conflicts with the proposed model. Lindsay et al. (2005) had proposed an andesitic source for the southern deposits on Dominica, with variations due to different degrees of differentiation. However, we found deposits with similar silica content could be distinguished by their apatite chemistry. KH-4 has overlapping zircon rim ages with RI-10 and RI-9 (Figure 4), as well as a similar silica content (Figure 11). However, the KH-4 apatites are much higher in La/Nd, Sr/Y, and Sm/Dy, which correspond to a higher LREE/HREE ratio. The oxygen fugacity of KH-4 was higher than other samples, at values of ΔNNO 0.86 compared to the other samples at ΔNNO ~0.37. Thus, the differences between these deposits cannot be explained by different stages of evolution, as proposed by Lindsay et al. (2005) and may be reflective of redox state, as previously found by (Watson and Green, 1981; Roeder et al., 1987).

Lindsay et al. (2005) also found no petrologic or geochemical evidence of mafic recharge at the Play Pays volcanic center and suggested continued fractionation. With this proposed model, the eruptive deposits would become more evolved with age. However, we found that younger deposits from the Wotten Waven caldera region, including the Micotrin lava dome and ignimbrite RI-13, are less evolved than the older eruptions (Figure 11). The RI-13 pumice samples also have a different trace element signature (Figure 14), a more variable bulk rock chemistry (Figure 12, 13), and apatite chemistry lower in LREE/HREE ratios compared to the other samples (Figure 19, 20). Thus there appears to have been a fundamental change in the source between ~20 ka (Link Flows) and the eruptions associated with Micotrin/Casso (RI-13) ~1 ka.

Overall, the apatite chemistry showed that the different eruptive events could be distinguished from one another, even with similar silica content. This is exemplified by how the apatite chemistry of KH-4 was distinctively higher in LREE/HREE ratios compared to RI-10 and RI-9, which have similar silica content. This contrasts with the idea that they crystallized from a homogeneous magma body. Numerous studies have linked the chemistry of apatite to reflect the conditions under which they crystallized. The REE composition of apatite can be directly correlated to the general rock type, temperature, and silica content of their host rock (Tieber et al., 2015, Chu et al., 2009). However, samples in the Roseau Valley do not appear to have a correlation between silica composition and apatite composition. For example, RI-13 is the least evolved magma at 58-60 wt. % SiO_2, but has apatite compositions similar to other deposits up to 61-64 wt% SiO_2 (Figure 21).

The partitioning of REE into the apatite structure has been linked to the oxidation state of the reservoir (Watson and Green, 1981; Roeder et al., 1987). The partition of REE into apatite may also be affected by the crystallization of other REE-bearing minerals (Chu et al., 2009). However, there is no variation in mineral assemblages from sample to sample on Dominica (Flake, 2014; Brehm, 2015) so the varying apatite chemistry we see is likely unrelated to mineral phases.

Chu et al. (2009) conducted a broad study investigating apatite's relationship to the host rock. They found that Sr, REE, and Eu anomalies in apatite have a direct relationship to the parent magma composition. However in some cases the REE and Sr signatures were inconsistent with the host rock silica content. They proposed REE and Sr patterns inconsistent with silica content are indicators of magma and compositional heterogeneity in the source reservoir. This suggests that variations in Sr content between samples in the Roseau Valley may be due to magma mixing or crustal influences (Chu et al., 2009).

A comparison of WR Sr content to apatite Sr content showed that the apatites had higher concentrations of Sr than their host rocks. Since Sr content in magma declines with evolution, apatite grains that have higher Sr content than their WR may indicate that mafic magmas were involved in magma formation (Chu et al., 2009). This observation may provide support for mafic recharge into the system before the young pyroclastic eruption of RI-13, which has the highest Sr content. Babiak (2015) suggested that a mafic injection triggered the eruption of the RI-13. This is supported by the low silica content of this deposit compared to older eruptions. This eruption, dated at 2-6 ka, may also be related to the emergence of the Micotrin lava dome at 1,082 +/-68 years BP. Therefore, the eruption which created RI-13 may have been triggered by a mafic injection and the rejuvenation of the Micotrin volcanic center.

Interpretation of Apatite Textures

Since apatite composition has been shown to reflect magmatic conditions, changes in apatite chemistry likely reflect changing magmatic conditions. REE zoning in apatite crystals be linked to variations in the composition and temperature of the host magma (Dempster et al., 2003; Tepper and Keuhner, 1999). The variation of apatite CL textures between samples then suggests that these crystals have separate crystallization histories and ascent paths. All the samples commonly have oscillatory zoning, but other zoning characteristics distinguish the samples. KH-4 has 30% dark cores, RI-15 has 32% irregular cores, and RI-13 has 36% bright rims (Table 1). Since the textural categories are related to magmatic composition and processes, the various textural patterns in the samples suggest they crystallized under geochemically diverse conditions.

RI-15, RI-13, and KH-4 contain irregular cores. These cores contained dissolution textures, and did not reflect the broader crystallographic shape. These cores could be inherited cores from early phases of crystallization, possibly re-dissolving and acting as nuclei for later growth (Dempster et al., 2003). Another process could be the incorporation of crustal or residual material into the magma during ascent. One possible explanation is that there was residual material from a previous eruption, which the younger magma rose through during its ascent (Figure 25).

The residual melt hypothesis agrees with the zircon populations of RI-13. RI-13 has a young age population at 3+/-8 ka, and an older population at ~80-200 ka (Figure 4). This older population overlaps with the age populations of older deposits in the Roseau

Valley, such as KH-4, RI-9 or RI-10. If the rising magma incorporated the apatites, it could have also incorporated the non-erupted zircons from the residual melt. Subsequently, the apatites grew rims on pre-existing cores/nucleation surfaces, whereas the zircons did not, which results in the myriad of ages seen in the PD plots (Figure 4).

However, RI-15 which contains the most irregular cores, does not contain an older zircon population, exhibiting a unimodal peak ~20-30 ka (Fig. 4). One possible explanation is that we simply did not analyze the older zircons, since only 12 grains were analyzed. Alternatively, RI-15 could have undergone a different process leading to these cores, or RI-15 could have ascended through younger residual material with distinctive apatites, but a similar zircon population.

Due to the spot size of the laser on the ICP-MS and the grain size of the apatite crystals, we were unable to document core to rim changes in chemistry. Almost entire grains were ablated, recording the chemistry of the core and the rim together. This limits our ability to test the hypothesis of inherited cores since we were unable to determine if the cores have a distinctive REE signature compared to the rims. We found few distinctions between the apatite grains with irregular cores and those without. The only difference is that the irregular core grains were generally lower in Sr/Y, but showed no pattern in other REE ratios (Figure 19, 20).

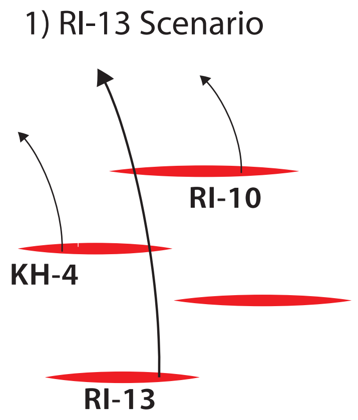

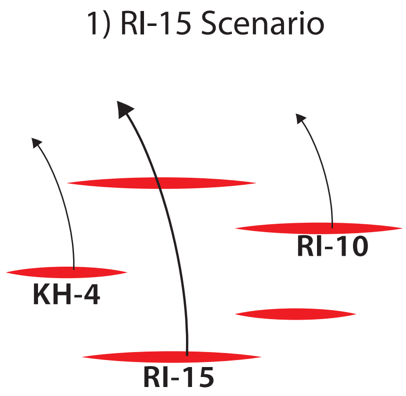

Figure 25. Illustration of the proposed hypothesis of irregular cores in RI-13 and RI-15. RI-13 could have ascended through residual material of the older eruptions, while RI-15 may ascended through other material.

Chlorine-Fluorine Zoning and Magmatic Processes

Another texture we found in CL was the streaky and radial zoning in RI-9 and RI-10. Since the bright streaks in CL corresponded to bright chlorine streaks in elemental mapping, we propose that this streaky zoning in CL is related to the preferential diffusion of halogens and perhaps some of the REE CL activators, in the apatite crystals. The crystals had chlorine rich streaks along the c-axis, but their cores were enriched in chlorine and their rims were depleted in fluorine. HCl and HF are common volatiles released from volcanoes during degassing.

A possible explanation for the core to rim enrichment of fluorine is that the magma was degassing upon ascent. Fluorine preferentially partitions in the apatite structure, and it's compatibility with apatite increases with decreasing temperature (Tieber et al, 2015; Mathez and Webster, 2004). Chlorine also escapes from the melt during eruptions and cooling (Mathez and Webster, 2004). This would require that there was a longer post-crystallization residence time, possibly from following a slower ascent path. This would allow the magma to de-gas as the crystals were still at temperatures allowing for halogen diffusion (Boyce et al., 2008). The magma could have been degassing HCl, causing the crystals to re-equilibrate with the melt, substituting fluorine for chlorine in its structure. Halogens can migrate in the apatite structure up to 5x faster than cathodoluminescence causing REE, explaining why CL patterns were still retained while halogens may have undergone diffusion (Boyce et al.; Brenan, 1993; Cherniak, 2000).

Another explanation could be that the apatite grains were altered in a post-eruption process. RI-10 is a welded sample, meaning it was at the bottom of a pyroclastic flow and stayed hot after the eruption due to thermal insulation. The sample from RI-9 was also taken near the bottom of a ~20 meter ignimbrite. The apatite grains in these samples could have been hotter for longer due to thermal insulation post-eruption, allowing for the diffusion of volatile elements to a volatile-depleted, cooling pyroclastic flow in a similar process to degassing during storage. Further investigations into halogens and volatiles in apatite would require quantitative data from an instrument such as the ion microprobe. Recording volatile stratigraphies of apatite grains similar to Boyce et al.'s 2008 study could help to determine if volatile behavior is an important factor in eruption triggers or magma ascent for Dominican Volcanoes.

Proposal of Multiple Magma Batches

Before suggesting a single batholith model, Smith et al. (2013) described an alternative magma storage model, which would produce chemically distinct magma batches. They discounted this model on the basis that the deposits on Dominica are geochemically homogeneous. This alternative model involved the pooling of magma at density discontinuities in the lithosphere (Menand et al., 2011). These batches of magma may be trapped and independently differentiate during storage. These pools may also form barriers which rising magma will bypass, and reach the surface through a different route. Such a process would create chemically distinct volcanoes (Smith and Roobol, 1990), each with their own volcanic systems. This model supports our hypothesis of the irregular cores in RI-13. As RI-13 rose to the surface, it came in contact with un-erupted or residual material, inheriting apatite cores and zircon grains.

Overall, the apatite textures between samples shows that they underwent various crystallization histories and ascent paths. The apatite chemistry also provides evidence that the apatites crystallized in distinct magma bodies. A model proposed by Cashman et al. (2017) describes a vertically (rather than horizontally i.e. Smith et al., 2013) extensive magma storage system beneath volcanoes. These storage systems consist of stacked sills throughout the mid crust, which are heterogeneous in composition, space and time (Figure 26). A model for Dominican volcanoes with heterogeneous, ephemeral sills is supported by the apatite chemistry and textures.

This model also involves the potential for transient vertical connectivity, allowing for mafic injections into the mid or upper crust (Cashman et al., 2017). This vertical connectivity could explain the variable bulk chemistry and lower silica content of RI-13. Magma mixing between an andesite mush and a basaltic injection could produce these characteristics of RI-13. Since RI-13 is less evolved, there must have been some kind of mafic input into the system, which vertical connectivity can explain.

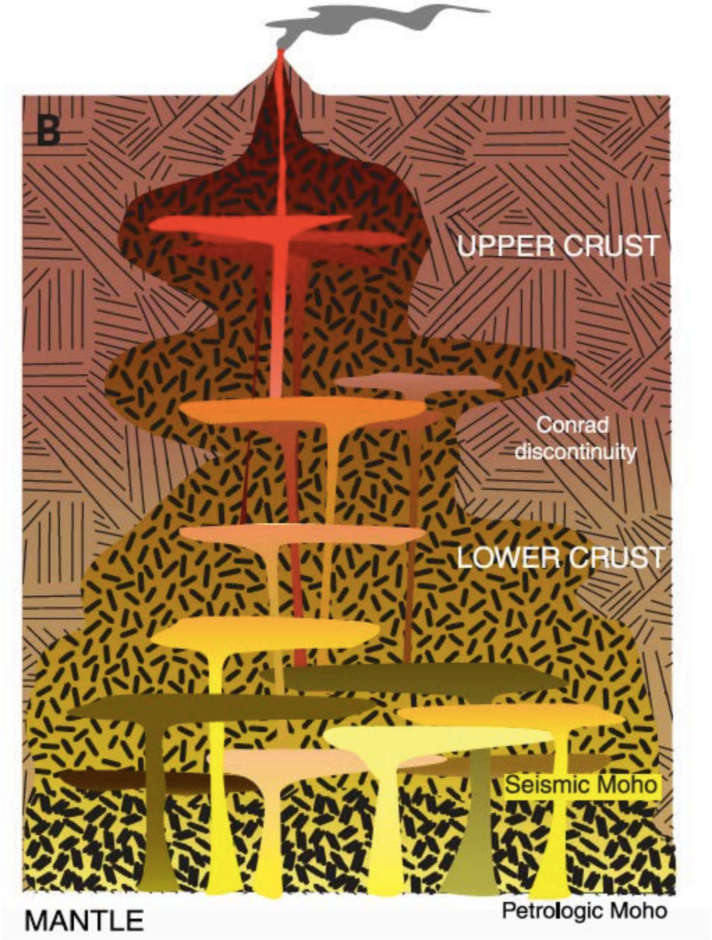

Figure 26. A more modern proposed model of magma chamber morphology involved semi-related or independently crystallizing melt pockets or sills, which are intermittently connected to the deeper crust and undergoing magma mixing (Cashman et al, 2017).

The batholith model for Dominica can help to explain some of the unique aspects of the island, for example its numerous volcanic centers and geochemically similar deposits. However, we suggest that there is a more complicated vertical magma storage system beneath the island, composed of multiple magma chambers and ephemeral sills. There is also the potential for vertical connectivity to the deep crust, supported by the younger and less evolved composition of RI-13.

CONCLUSIONS

1) Using apatite REE chemistry we were able to fingerprint different eruptive events on Dominica, proving apatite to be a valuable tool in characterizing volcanic deposits with similar bulk-rock chemistry.
2) The variable REE compositions of apatite grains between samples, which have similar bulk rock chemistry and chronology, indicates that the magma supplying the different eruptive events is chemically distinct.
3) Apatite zoning textures in CL indicate variable REE and trace element patterns between samples. This may indicate the apatite crystals had different ascent paths and crystallization histories.
4) Apatite REE and Sr compositions do not reflect the whole rock chemistry of the deposits, which has been previously attributed to magma mixing, mafic inputs, and crustal influences (Chu et al., 2009).
5) The data presented in this study conflicts with a hypothesis of a single, homogenous magma chamber beneath the island, presented by Smith et al. (2013) and Howe et al. (2015). The apatite chemistry and textures suggest that they crystallized from chemically distinct magmas, suggesting that the magma storage system may be composed of smaller, ephemeral sills and magma batches. We suggest the magmatic system beneath Dominica is not a horizontally homogeneous magma body, but rather that the volcanic centers may have semi-related vertical storage systems with the potential for vertical connectivity (Cashman et al., 2017).

6) The most recent reactivation of the Micotrin volcanic center may have been initiated by a mafic injection and/or vertical connectivity of the system. This event could have triggered the relatively mafic eruptive deposit at Casso (RI-13) at 2-6 ka.

REFERENCES

Annen, C.. 2011. Implications of incremental emplacement of magma bodies for magma differentiation, thermal aureole dimensions and plutonism–volcanism relationships. Tectonophysics 500.1: 3-10.

Babiak, R., 2015. Reconstructing the eruptive history of Dominica using U-Th disequilibrium dating of zircon rims. Union College senior thesis, Schenectady, New York.

Bellon, H., 1988. Reconnaissance chronologique des deux premieres phases d’activite volcanique en Dominique (Petites Antilles). CR Acad Sci Paris 306:1487-1492

Boyce, J. and Hervig, R., 2008. Magmatic degassing histories from apatite volatile stratigraphy. Geology 36.163-66.

Boyce, J. and Hervig, R., 2009. Apatite as a monitor of late-stage magmatic processes at Volcán Irazú, Costa Rica. Contributions to Mineralogy and Petrology 157.2: 135-145.

Brehm, S., 2015. Using zircon geochronology and apatite tephra fingerprinting to understand the origin of ignimbrites on Dominica. Union College senior thesis, Schenectady, New York.

Brenan, J., 1993, Kinetics of fluorine, chlorine, and hydroxyl exchange in fuorapatite: Chemical Geology, v. 110, p. 195–210.

Cashman, K. et al., 2017. Vertically extensive and unstable magmatic systems: A unified view of igneous processes. Science 355.6331: eaag3055.

Cherniak, D.J., 2000, Rare earth element diffusion in apatite: Geochimica et Cosmochimica Acta, v. 64, no. 22, p. 3871–3885.

Chu, Mei-Fei, et al., 2009. Apatite composition: tracing petrogenetic processes in Transhimalayan granitoids." Journal of Petrology 50.10: 1829-1855.

Couch, S. et al., 2001. Mineral disequilibrium in lavas explained by convective self-mixing in open magma chambers. Nature 411.6841: 1037-1039.

Demange, J. et al., 1985. Histoire Volcano Structurale De La Region Sud de la Dominique. Institute Mixte Recherches Geothermiques: Orleans, France.

Dempster, T. J., et al., 2003. Magmatic zoning in apatite: a monitor of porosity and permeability change in granites. Contributions to Mineralogy and Petrology145.5: 568-577.

Flake, A., 2014. Correlating monotonous crystal-rich dacitic ignimbrites in Dominica: the Layou and Roseau Ignimbrite. Union College senior thesis, Schenectady, New York.

Fournier, N., et al., 2009. "Boiling Lake of Dominica, West Indies: High-temperature volcanic crater lake dynamics." Journal of Geophysical Research: Solid Earth 114.B2.

Glazner, A. et al., 2004. Are plutons assembled over millions of years by amalgamation from small magma chambers? GSA today 14.4/5: 4-12.

Harlov, D., 2015. Apatite: a fingerprint for metasomatic processes. Elements 11.3: 171-176.

Howe, T. et al., 2015. Evolution of young andesitic–dacitic magmatic systems beneath Dominica, Lesser Antilles. Journal of Volcanology and Geothermal Research 297: 69-88.

Howe, T. M., et al., 2015. Time scales of intra-oceanic arc magmatism from combines U-Th and (U/Th)/He zircon geochronology of Dominica, Lesser Antilles. Geochemistry, Geophysics, Geosystems 16.2: 347-365.

Howe, T. M., et al., 2014. Re-evaluation of the Roseau Tuff eruptive sequence and other ignimbrites in Dominica, Lesser Antilles. Journal of Quarternary Science 29.2: 531-546.

Hughes, John M., and John F. Rakovan. 2015. Structurally robust, chemically diverse: apatite and apatite supergroup minerals. Elements 11.3: 165-170.

Lindsay, J. et al., 20015. Geochemistry and Petrogenesis of Late Pleistocene to Recent Volcanism in Southern Dominica, Lesser Antilles. Journal of Volcanology and Geothermal Research 148.3-4: 253-94. Web.

Martin-Kaye, P.H.A., 1956-1961, Geological Survey of the Windward Islands. Unpubl. Progress Reports of the Government Geologist. Nos. 1-12.

Mathez, Edmond A., and James D. Webster. 2005. Partitioning behavior of chlorine and fluorine in the system apatite-silicate melt-fluid. Geochimica et Cosmochimica Acta 69.5: 1275-1286.

Menand, T., 2011. Physical controls and depth of emplacement of igneous bodies: A review. Tectonophysics 500.1: 11-19.

Prowatke, Stefan, and Stephan Klemme., 2006. Trace element partitioning between apatite and silicate melts. Geochimica et Cosmochimica Acta 70.17: 4513-4527.

Roeder, Peter L., et al., 1987. Cathodoluminescence and microprobe study of rare-earth elements in apatite. American mineralogist 72.7-8: 801-811.

Samson, S. et al., 1988. Correlation of North American Ordovician bentonites by apatite chemistry: Geology, 16. 444-447.

Scott, Jeannie AJ, et al., 2015. "Insights into the behaviour of S, F, and Cl at Santiaguito Volcano, Guatemala, from apatite and glass." Lithos 232: 375-394.

Seismic Research Unit, 2000. Volcano Hazard Report for Southern Dominica: Interpretation of 1998-2000 Earthquakes and Hazard Mapping Results.

Sell, Bryan Keith, and Scott Douglas Samson., 2011. "A tephrochronologic method based on apatite trace-element chemistry." Quaternary Research 76.1: 157-166.

Shaw, George H., 2003. Trace element chemistry of individual apatite phenocrysts as a tool for fingerprinting altered volcanic ash beds: Assessing interbed and intrabed variation at local and regional scales. Geological Society of America Bulletin 115.8 : 933-942.

Sigurdsson, H., and S. N. Carey., 1991. Caribbean volcanoes: a field guide to Martinique, Dominica and St. Vincent. Geological Association of Canada, Field Trip Guidebooks: 1-101.

Sigurdsson, H., 1972. Partly-welded pyroclast flow deposits in Dominica, Lesser Antilles. Bulletin Volcanologique 36.1: 148-163.

Smith, A. L., et al., 2013. The Volcanic Geology of the Mid-Arc Island of Dominica, Lesser Antilles—The Surface Expression of an Island-Arc Batholith. *Geological Society of America Special Papers* 496: 1-2.

Stock, Michael J., et al., 2015. New constraints on electron-beam induced halogen migration in apatite. American Mineralogist 100.1: 281-293.

Stock, M., et al., 2016. Late-stage volatile saturation as a potential trigger for explosive volcanic eruptions. Nature Geoscience 9.3: 249-254.

Stormer, J.et al., 1993. Variation of F and Cl X-ray intensity due to anisotropic diffusion in apatite. American Mineralogist 78: 641-648.

Wadge, G., Shepherd, J.B., 1984. Segmentation of the Lesser Antilles subduction zone. Earth Planet. Sci. Lett. 71 (2), 297–304.

Watson, E. Bruce, and Trevor H. Green., 1981. Apatite/liquid partition coefficients for the rare earth elements and strontium. Earth and Planetary Science Letters 56: 405-421.

Webster, James D., and Philip M. Piccoli., 2015. Magmatic apatite: a powerful, yet deceptive, mineral. Elements 11.3: 177-182.

APPENDIX

Table 1. Whole rock geochemistry, major oxides (wt. %) and trace elements (ppm), concentrations.

	SiO_2	Al_2O_3	Fe_2O_3	MgO	CaO	Na_2O	K_2O	TiO_2	P_2O_5	MnO	Ba	Sr	Zr	Y
RI-9D	62.1	16.9	6.4	2.4	6.4	3.5	1.5	0.5	0.1	0.1	220.0	207.0	87.0	17.0
RI17	59.6	17.3	8.4	3.1	6.4	2.9	1.2	0.6	0.1	0.2	211.0	220.0	77.0	17.0
RI18	62.6	16.9	6.7	2.4	5.9	3.1	1.6	0.5	0.1	0.2	268.0	214.0	91.0	19.0
RI19	63.2	16.9	6.1	2.2	6.0	3.2	1.6	0.5	0.1	0.2	258.0	208.0	85.0	17.0
RI20	61.2	17.9	7.3	2.5	6.0	3.0	1.3	0.6	0.1	0.2	241.0	217.0	81.0	17.0
RI-10C	63.1	17.0	6.1	2.2	6.0	3.3	1.6	0.5	0.1	0.1	245.0	209.0	97.0	17.0
RI21	60.1	18.9	9.1	3.1	4.2	2.3	1.3	0.7	0.1	0.2	242.0	183.0	82.0	17.0
RI22	55.8	19.1	9.4	3.6	7.5	2.8	0.8	0.7	0.1	0.2	156.0	227.0	68.0	19.0
RI-13C	58.7	17.2	8.4	3.4	6.9	3.4	1.1	0.6	0.1	0.2	181.0	221.0	73.0	25.0
RI-13	59.8	16.8	7.7	3.2	6.5	3.9	1.2	0.6	0.1	0.2	210.0	213.0	75.0	16.0
RI-13B	58.2	16.7	8.0	3.3	6.5	3.8	1.2	0.6	0.1	0.2	209.0	215.0	72.0	15.0
RI-13C	58.7	16.9	7.9	3.4	6.6	3.8	1.2	0.6	0.1	0.2	212.0	219.0	74.0	15.0
RI-14B	59.3	17.7	8.7	3.0	6.1	3.0	1.2	0.6	0.1	0.2	184.0	207.0	75.0	16.0
RI16	60.4	17.6	7.3	2.8	6.5	3.2	1.3	0.6	0.1	0.2	242.0	234.0	78.0	17.0
MI-1A	61.4	17.2	6.8	2.6	6.6	3.3	1.3	0.6	0.1	0.2	245.0	228.0	84.0	17.0
MI-1B	60.7	17.1	7.3	2.8	6.8	3.1	1.3	0.6	0.1	0.1	232.0	225.0	86.0	18.0
MI-1C	60.4	17.3	7.4	2.8	6.8	3.2	1.3	0.6	0.1	0.2	219.0	227.0	80.0	16.0
MI-1C	61.3	17.6	7.4	2.8	6.9	3.3	1.3	0.6	0.1	0.2	233.0	227.0	84.0	16.0
RI-10	60.1	17.0	7.9	3.2	6.6	3.0	1.2	0.6	0.1	0.2	215.0	220.0	78.0	15.0
RI-10B	63.6	17.0	6.7	2.4	6.1	3.3	1.6	0.5	0.1	0.1	264.0	210.0	102.0	16.0
RI-10C1	61.4	17.4	7.5	2.9	6.6	3.2	1.3	0.6	0.1	0.2	232.0	220.0	80.0	16.0
RI-10C2	60.7	17.2	8.1	3.1	6.7	3.2	1.3	0.6	0.1	0.2	220.0	219.0	80.0	16.0
RI-9A	62.7	16.7	6.3	2.4	6.1	3.5	1.6	0.5	0.1	0.1	254.0	206.0	94.0	20.0
RI-9B	62.6	16.6	6.3	2.4	6.1	3.6	1.6	0.5	0.1	0.1	249.0	207.0	90.0	20.0
RI-9C	61.9	16.7	6.8	2.6	6.4	3.4	1.5	0.5	0.1	0.2	240.0	210.0	90.0	18.0
KH-1A	63.7	16.8	5.9	2.1	5.9	3.2	1.7	0.5	0.1	0.1	268.0	219.0	104.0	15.0
KH-1B	62.2	17.1	6.4	2.6	6.2	3.1	1.5	0.5	0.1	0.1	254.0	224.0	90.0	17.0
KH-2A	63.0	16.8	6.3	2.4	5.9	3.2	1.6	0.5	0.1	0.2	266.0	219.0	92.0	15.0
KH-2B	62.4	16.9	6.5	2.4	6.2	3.2	1.6	0.5	0.1	0.1	251.0	224.0	85.0	16.0
KH-2C	63.3	16.8	6.1	2.2	6.0	3.2	1.6	0.5	0.1	0.1	264.0	219.0	90.0	16.0
KH-3A	63.2	16.6	6.1	2.3	5.9	3.5	1.6	0.5	0.1	0.1	261.0	219.0	92.0	16.0
KH-3B	61.9	16.7	6.7	2.6	6.2	3.5	1.5	0.6	0.1	0.2	242.0	221.0	79.0	16.0
KH-4A	61.8	16.7	7.2	2.8	6.0	3.2	1.5	0.5	0.1	0.2	241.0	212.0	88.0	16.0
KH-4B	62.3	16.9	6.8	2.5	6.0	3.2	1.5	0.5	0.1	0.2	245.0	217.0	88.0	16.0
KH-4C	62.1	16.6	7.0	2.7	6.0	3.2	1.5	0.5	0.1	0.2	244.0	215.0	90.0	16.0
RI-1A	63.0	16.6	6.2	2.5	6.1	3.4	1.6	0.5	0.1	0.1	264.0	220.0	92.0	16.0

RI-1B	63.6	16.8	5.7	2.2	6.0	3.4	1.6	0.4	0.1	0.1	262.0	215.0	95.0	15.0
RI-1C	65.2	16.5	5.2	1.9	5.6	3.2	1.7	0.4	0.1	0.1	288.0	211.0	93.0	16.0
RI-2	64.1	16.6	5.3	2.1	5.9	3.5	1.7	0.5	0.1	0.1	275.0	214.0	98.0	18.0
RI-3	63.8	16.7	5.8	2.2	5.8	3.3	1.7	0.4	0.1	0.1	279.0	216.0	95.0	17.0
RI-2B	62.8	16.4	6.3	2.5	6.0	3.6	1.7	0.5	0.1	0.1	266.0	214.0	103.0	17.0
RI-2C	63.1	16.3	6.3	2.5	5.9	3.4	1.7	0.5	0.1	0.2	273.0	210.0	96.0	17.0
RI-3B	62.8	16.7	6.4	2.4	5.9	3.3	1.7	0.5	0.1	0.2	261.0	218.0	99.0	17.0
RI-3C	63.3	16.4	6.3	2.4	5.8	3.3	1.7	0.5	0.1	0.2	268.0	212.0	94.0	16.0
RI-3D	62.5	17.0	6.3	2.2	6.1	3.4	1.6	0.5	0.1	0.1	258.0	226.0	85.0	17.0
RI-15A	61.8	16.8	6.9	2.5	6.1	3.4	1.6	0.5	0.1	0.2	246.0	208.0	89.0	17.0
RI-15B	62.5	17.2	6.3	2.3	6.1	3.2	1.6	0.5	0.1	0.1	256.0	206.0	95.0	18.0
RI-15C	62.7	17.1	6.3	2.3	6.1	3.2	1.6	0.5	0.1	0.1	257.0	205.0	93.0	17.0
RI-15D	62.1	17.0	6.8	2.4	6.0	3.3	1.6	0.5	0.1	0.1	245.0	204.0	89.0	18.0
RI-15E	58.9	17.6	8.0	3.2	6.8	3.2	1.3	0.6	0.1	0.2	210.0	220.0	75.0	16.0

Table 2. Whole rock rare earth element concentrations in ppm.

Sample	**La**	**Ce**	**Pr**	**Nd**	**Sm**	**Eu**	**Gd**	**Tb**	**Dy**	**Ho**	**Er**	**Tm**	**Yb**	**Lu**
Chondrite Normalizing Values	0.237	0.613	0.092	0.457	0.148	0.0563	0.199	0.036	0.246	0.054	0.16	0.024	0.161	0.024
KH-1A	47.1	36.2	29.5	24.0	17.2	14.0	12.9	11.4	10.8	10.3	10.4	10.5	11.4	12.6
KH-1B	49.5	38.9	32.9	27.6	19.5	14.6	14.9	13.3	12.3	11.9	11.7	12.1	12.6	14.2
KH-2A	45.9	35.2	28.6	23.9	17.0	13.9	13.1	11.6	10.8	10.4	10.4	10.5	11.5	12.6
KH-2B	45.1	34.4	28.8	23.7	17.1	14.2	13.1	11.4	10.9	10.6	10.4	10.9	11.5	13.0
KH-2C	48.1	69.9	30.4	25.2	17.6	14.6	11.7	11.9	11.4	11.4	11.0	11.3	12.2	13.4
KH-2Cb	46.7	39.6	29.0	24.4	17.4	13.9	12.9	11.9	11.1	11.0	10.8	11.3	12.0	13.0
KH-2Cc	46.3	38.2	29.0	24.2	17.8	14.4	13.1	11.9	11.3	11.4	11.1	11.3	12.2	13.8
KH-3Aa	47.5	37.5	29.7	25.3	17.6	14.2	13.6	11.9	11.5	11.2	11.2	11.3	12.0	13.4
KH-3Ab	45.6	36.0	28.7	23.9	16.6	13.7	12.9	11.4	10.8	10.4	10.5	10.9	11.4	13.0
KH-3Ac	46.0	35.2	28.7	23.7	16.8	14.0	13.0	11.9	11.0	10.6	10.9	10.9	11.8	13.0
KH-3B	46.3	36.5	30.0	24.5	18.4	14.9	15.0	13.3	12.5	12.1	12.0	12.1	12.7	14.2
KH-4A	46.2	36.5	30.6	25.6	18.6	14.2	14.6	13.0	12.3	11.9	11.8	12.1	12.8	14.6
KH-4B	45.9	35.9	29.4	25.2	17.7	14.0	13.8	12.2	11.6	11.2	11.2	11.3	12.3	13.4
KH-4C	45.4	70.6	28.9	24.8	17.0	13.7	11.3	11.9	11.0	11.0	10.9	11.3	11.9	13.0
12D-RI-1A	47.2	36.0	29.4	23.8	16.5	13.3	13.6	11.9	11.1	11.0	11.1	10.9	12.0	8.5
12D-RI-1A-2	47.7	36.1	29.5	24.9	17.5	14.0	13.5	11.6	10.8	10.8	10.8	10.9	11.8	13.4
12D-RI-1A-3	46.6	36.1	29.1	24.4	17.2	14.2	13.6	11.9	11.1	11.0	10.9	11.3	11.6	13.0
12D-RI-1B	42.4	32.2	26.8	21.6	15.1	12.4	12.5	11.1	10.6	10.3	10.3	10.1	10.9	6.9

12D-RI-1C	48.4	36.6	29.5	24.1	16.6	13.5	13.9	11.9	11.1	11.2	11.2	10.9	12.0	8.9
12D-RI-2	45.1	32.8	29.7	24.3	17.0	13.3	14.0	12.2	11.5	11.2	10.9	10.9	11.6	8.1
12D-RI-3	49.1	36.3	31.9	26.4	18.3	14.0	14.5	12.7	12.3	11.9	11.8	11.7	12.7	10.2
RI-1A	45.8	34.9	28.3	23.8	16.9	13.9	13.2	11.9	11.1	10.8	10.7	10.9	11.8	13.0
RI-1B	46.1	34.6	28.2	23.5	17.1	14.0	13.2	11.9	11.2	10.6	10.9	10.9	12.0	13.4
RI-1C	48.9	37.4	30.6	25.2	17.5	14.2	13.5	11.9	11.2	11.2	11.1	11.3	12.3	13.8
RI-2B	49.7	37.8	32.4	27.6	19.7	14.9	15.1	13.3	12.3	12.1	11.9	12.1	13.0	14.2
RI-2C	49.2	36.4	31.4	26.9	18.9	14.6	14.7	13.0	12.0	11.7	11.4	11.7	12.6	13.8
RI-3B	48.1	36.7	30.8	26.4	18.4	14.6	14.3	12.7	11.7	11.2	11.1	11.3	12.5	13.8
RI-3B	47.4	35.6	30.4	25.7	18.6	14.6	14.8	12.7	11.7	11.7	11.6	11.7	12.4	14.2
RI-3C	48.2	36.4	30.4	26.1	18.1	14.4	14.3	12.7	11.7	11.4	11.3	11.3	12.4	13.8
RI-3D	47.6	35.7	30.4	26.0	18.7	14.7	14.6	13.0	12.2	11.7	11.4	11.7	12.5	13.8
RI9B	30.7	26.2	28.8	26.5	20.3	14.6	16.1	11.9	10.7	10.1	9.8	9.7	10.6	11.8
RI9C	50.7	39.4	43.0	37.0	28.8	21.0	20.9	16.9	14.8	13.7	13.3	13.4	14.7	16.3
RI10A	52.4	42.0	44.5	38.8	25.1	20.4	19.0	15.0	13.5	12.6	12.5	13.0	13.8	15.9
RI10C1	52.8	42.2	44.6	39.3	24.7	20.1	18.5	15.0	13.3	12.3	11.8	12.6	13.4	15.0
RI10C2	52.9	42.3	44.5	39.6	25.4	20.8	19.1	15.5	13.8	12.8	12.5	13.0	14.2	16.3
RI13B	51.8	41.0	44.6	39.5	25.5	20.6	19.1	15.2	13.7	13.0	12.5	13.0	14.1	15.9
RI13C	50.4	39.1	43.0	37.7	25.3	20.2	19.0	15.0	13.7	12.6	12.3	12.6	13.7	15.9

Table 3. Single apatite grain rare earth element concentrations in ppm with Sr/Y, Ce/Lu, La/Nd, Yb/Dy, and Sm/Dy ratios.

	Sr	**Y**	**La**	**Ce**	**Pr**	**Nd**	**Sm**	**Eu**	**Gd**	**Dy**	**Yb**	**Lu**	**Pb**	**Th**	**U**	**Sr/Y**	**Ce/Lu**	**La/Nd**	**Yb/Dy**	**Sm/Dy**
KH4-16	387	929	935	2082	278	1383	237	28	251	174	64	9	2	28	9	0.4	231.3	0.7	0.4	1.4
KH4-17	392	809	967	1976	269	1300	218	25	209	138	55	8	3	24	8	0.5	247.0	0.7	0.4	1.6
KH4-19	415	876	895	2090	282	1454	236	28	225	163	60	9	2	27	10	0.5	232.2	0.6	0.4	1.4
KH4-20	406	884	879	1828	245	1296	213	27	204	149	58	9	2	19	8	0.5	203.1	0.7	0.4	1.4
KH4-22	373	1049	820	1925	276	1352	269	28	270	210	67	9	3	31	9	0.4	213.9	0.6	0.3	1.3
KH4-23	392	845	937	2129	264	1440	211	27	221	156	59	9	2	29	10	0.5	236.6	0.7	0.4	1.4
KH4-25	404	880	953	2123	271	1415	225	26	217	157	61	9	2	27	10	0.5	235.9	0.7	0.4	1.4
KH4-26	393	758	936	2183	281	1405	210	26	209	150	58	9	3	28	10	0.5	242.6	0.7	0.4	1.4
KH4-27a	427	1380	1641	3387	477	2234	364	45	339	244	100	15	3	50	19	0.3	225.8	0.7	0.4	1.5
KH4-27b	426	872	1009	2073	270	1476	230	27	211	156	62	9	2	31	10	0.5	230.3	0.7	0.4	1.5
KH4-28	404	750	863	1979	245	1372	209	26	200	143	53	8	2	26	10	0.5	247.4	0.6	0.4	1.5
KH4-29	398	724	856	2092	264	1433	212	28	200	143	54	8	2	23	9	0.5	261.5	0.6	0.4	1.5
KH4-30	412	751	883	2265	278	1466	203	25	183	143	54	8	3	20	9	0.5	283.1	0.6	0.4	1.4

KH4-31a	428	692	818	1957	242	1274	188	22	180	133	48	7	2	8	5	0.6	279.6	0.6	0.4	1.4
KH4-31b	405	991	835	1722	255	1374	254	27	268	195	63	10	2	17	6	0.4	172.2	0.6	0.3	1.3
KH4-32	432	876	1001	2173	290	1509	230	28	226	170	61	9	3	31	11	0.5	241.4	0.7	0.4	1.4
KH4-33a	388	838	829	2034	268	1407	224	27	216	153	57	8	2	26	9	0.5	254.3	0.6	0.4	1.5
KH4-33b	387	959	793	1855	242	1304	245	27	243	182	63	9	2	23	9	0.4	206.1	0.6	0.3	1.3
KH4-35	413	1121	1032	2293	307	1625	284	36	295	206	79	11	3	55	15	0.4	208.5	0.6	0.4	1.4
KH4-37a	372	631	806	1978	253	1283	181	24	173	119	46	7	2	21	8	0.6	282.6	0.6	0.4	1.5
KH4-37b	399	841	874	1945	260	1361	222	26	210	160	58	9	2	23	8	0.5	216.1	0.6	0.4	1.4
KH4-38	441	1165	980	2032	300	1602	284	32	292	222	75	11	2	33	11	0.4	184.7	0.6	0.3	1.3
KH4-1	381	832	724	1731	231	1186	208	26	208	159	56	8	2	24	8	0.5	212.6	0.6	0.4	1.3
KH4-12	373	748	854	2043	249	1290	192	23	169	126	49	7	2	22	8	0.5	286.8	0.7	0.4	1.5
KH4-15	365	885	727	1800	226	1187	207	24	211	158	52	7	1	18	7	0.4	259.6	0.6	0.3	1.3
KH4-2	373	708	888	2115	261	1337	196	24	178	131	50	8	2	28	10	0.5	277.8	0.7	0.4	1.5
KH4-6	358	609	636	1648	199	1020	151	19	150	112	38	5	2	15	7	0.6	310.4	0.6	0.3	1.3
KH4-8	369	559	794	2065	243	1199	155	19	135	99	38	6	2	14	7	0.7	371.4	0.7	0.4	1.6
RI13-11	362	1185	721	1693	247	1219	274	32	298	211	72	10	30	15	4	0.3	169.3	0.6	0.3	1.3
RI13-13	386	1035	568	1692	215	1197	276	31	278	226	71	10	3	21	7	0.4	169.2	0.5	0.3	1.2
RI13-3	278	955	474	1104	191	1010	214	23	251	202	65	9	6	14	3	0.3	122.7	0.5	0.3	1.1
RI13-35	377	1191	690	1449	221	1153	269	31	305	219	76	10	5	27	10	0.3	144.9	0.6	0.3	1.2
RI13-36	324	1376	634	1538	218	1265	306	25	357	265	81	10	44	28	4	0.2	153.8	0.5	0.3	1.2
RI13-4	443	1205	658	1449	234	1306	283	32	317	243	74	11	3	24	8	0.4	131.7	0.5	0.3	1.2
RI13-40	408	1276	598	1475	212	1220	271	32	286	222	77	10	2	14	5	0.3	147.5	0.5	0.3	1.2
RI13-47	394	1018	594	1648	213	1266	251	28	273	202	63	9	2	16	6	0.4	183.1	0.5	0.3	1.2
RI13-41	428	1362	733	1680	249	1428	326	33	356	278	83	12	4	22	6	0.3	140.0	0.5	0.3	1.2
RI13-43	311	911	460	1120	165	891	226	22	249	186	53	8	24	13	3	0.3	140.0	0.5	0.3	1.2
RI13-44	409	1404	632	1573	214	1229	303	33	336	268	81	11	5	22	7	0.3	143.0	0.5	0.3	1.1
RI13-46	457	1214	723	1662	253	1508	308	32	355	255	83	12	3	18	5	0.4	138.5	0.5	0.3	1.2
RI13-38	320	1209	643	1272	172	1114	244	28	279	230	62	9	5	12	4	0.3	141.3	0.6	0.3	1.1
RI13-1	386	1425	798	1835	294	1596	360	37	383	291	72	9	3	16	5	0.3	203.9	0.5	0.2	1.2
RI13-52	392	1322	651	1605	218	1230	301	36	352	262	83	12	2	18	6	0.3	133.8	0.5	0.3	1.1
RI13-9	417	1629	879	1888	308	1666	371	42	441	312	107	14	3	28	8	0.3	134.9	0.5	0.3	1.2
RI15-30	447	1321	847	1857	289	1560	306	34	314	253	80	12	2	22	6	0.3	154.8	0.5	0.3	1.2
RI15-21	355	874	495	1405	195	980	192	24	228	168	52	7	1	17	6	0.4	191.6	0.5	0.3	1.1
RI15-32	307	808	634	1224	193	1116	213	23	272	161	59	8	18	20	5	0.4	153.0	0.6	0.4	1.3
RI15-46	399	1031	701	1749	240	1266	243	27	264	200	68	9	2	19	8	0.4	194.3	0.6	0.3	1.2
RI15-4c	396	998	540	1612	227	1181	243	27	252	199	58	8	2	14	5	0.4	195.2	0.5	0.3	1.2
RI15-4r	350	869	496	1448	212	1036	213	24	235	171	53	7	2	11	5	0.4	203.6	0.5	0.3	1.2
RI15-55	419	1123	626	1638	232	1272	263	31	316	226	71	10	2	18	7	0.4	163.8	0.5	0.3	1.2

RI15-28	405	1217	658	1579	240	1308	286	32	309	239	72	11	2	16	6	0.3	143.5	0.5	0.3	1.2
RI15-10	388	1096	569	1615	225	1219	272	29	274	212	68	9	2	28	8	0.4	171.9	0.5	0.3	1.3
RI15-12	405	1245	708	1855	262	1381	294	31	327	247	80	11	3	21	7	0.3	170.0	0.5	0.3	1.2
RI15-13	406	1196	629	1628	238	1245	274	32	286	244	75	10	2	19	7	0.3	160.3	0.5	0.3	1.1
RI15-15	412	1506	683	1651	246	1329	327	36	376	276	93	12	2	17	5	0.3	135.3	0.5	0.3	1.2
RI15-17	355	1010	515	1574	220	1106	237	28	267	194	62	9	2	15	5	0.4	180.0	0.5	0.3	1.2
RI15-18	388	968	550	1530	210	1132	230	25	249	187	58	8	2	18	7	0.4	188.6	0.5	0.3	1.2
RI15-11	366	921	509	1396	199	1065	225	25	239	184	52	8	1	12	4	0.4	184.2	0.5	0.3	1.2
RI15-1	380	807	842	2193	259	1374	204	23	183	152	51	7	1	21	8	0.5	296.3	0.6	0.3	1.3
RI15-19	394	1215	612	1451	227	1120	289	29	319	247	75	11	2	22	7	0.3	133.3	0.5	0.3	1.2
RI15-2	360	820	561	1503	203	1072	205	23	214	158	53	8	2	11	4	0.4	200.0	0.5	0.3	1.3
RI15-20a	376	1082	574	1539	207	1119	231	27	265	197	62	9	3	13	5	0.3	180.2	0.5	0.3	1.2
RI15-20b	384	998	526	1459	218	1109	245	28	270	191	62	9	2	14	5	0.4	163.9	0.5	0.3	1.3
RI15-22	400	1462	663	1580	262	1397	336	38	392	284	89	12	2	18	5	0.3	131.7	0.5	0.3	1.2
RI15-25	334	827	448	1133	160	903	194	21	212	165	49	7	6	8	4	0.4	161.9	0.5	0.3	1.2
RI15-26	348	1043	586	1296	186	1068	220	25	252	193	61	8	2	16	5	0.3	162.0	0.5	0.3	1.1
RI15-3	385	1056	582	1579	248	1273	268	29	293	310	82	11	4	11	5	0.4	148.3	0.5	0.3	0.9
RI15-33	410	1217	736	1688	254	1408	314	35	339	260	79	12	3	23	7	0.3	140.7	0.5	0.3	1.2
RI15-34	401	1198	662	1632	235	1289	264	29	309	222	70	10	2	19	6	0.3	163.2	0.5	0.3	1.2
RI15-42	391	1146	618	1716	223	1232	287	33	304	223	72	10	2	15	6	0.3	171.6	0.5	0.3	1.3
RI15-43	351	949	779	1781	243	1249	249	25	307	192	66	7	3	16	6	0.4	254.4	0.6	0.3	1.3
RI15-44	416	1093	640	1667	231	1255	261	30	298	223	70	10	2	13	6	0.4	166.7	0.5	0.3	1.2
RI15-45	425	1286	644	1638	248	1330	292	34	335	250	81	11	2	26	8	0.3	148.9	0.5	0.3	1.2
RI15-47	382	1133	626	1477	218	1239	285	30	300	228	69	10	2	21	7	0.3	147.7	0.5	0.3	1.3
RI15-48	402	974	705	1780	248	1297	242	29	258	192	64	9	2	15	6	0.4	197.8	0.5	0.3	1.3
RI15-49	390	841	603	1639	221	1171	215	24	224	174	55	7	2	19	7	0.5	234.1	0.5	0.3	1.2
RI15-50	406	976	764	2011	267	1355	240	31	237	190	65	10	2	21	9	0.4	201.1	0.6	0.3	1.3
RI15-50b	408	890	589	1599	221	1149	221	27	239	184	59	8	2	15	6	0.5	199.9	0.5	0.3	1.2
RI15-51	410	1276	664	1474	220	1289	286	28	337	245	72	10	2	15	5	0.3	147.4	0.5	0.3	1.2
RI15-52	422	1055	603	1687	240	1277	272	30	297	218	69	10	2	13	6	0.4	168.7	0.5	0.3	1.2
RI15-56	402	1037	623	1866	253	1342	258	30	284	204	63	9	2	26	11	0.4	207.3	0.5	0.3	1.3
RI15-5c	371	788	756	1802	220	1129	177	24	173	145	60	8	1	23	9	0.5	223.1	0.7	0.4	1.2
RI15-5r	376	724	821	1914	229	1166	163	23	154	118	48	7	2	23	9	0.5	269.1	0.7	0.4	1.4
RI15-6	371	774	508	1325	179	916	174	21	192	147	45	7	2	15	7	0.5	199.1	0.6	0.3	1.2
RI15-7	383	828	614	1684	225	1125	210	25	220	161	57	8	2	14	5	0.5	220.3	0.5	0.4	1.3
RI15-8	368	910	558	1481	217	1142	230	25	223	176	56	8	2	15	7	0.4	181.3	0.5	0.3	1.3
RI15-9	376	932	488	1470	194	1059	230	25	234	186	57	8	2	13	5	0.4	176.5	0.5	0.3	1.2
RI10-11b	379	1130	600	1495	212	1176	241	27	274	210	66	9	2	15	5	0.3	163.0	0.5	0.3	1.1

RI10-11b	379	1130	600	1495	212	1176	241	27	274	210	66	9	2	15	5	0.3	163.0	0.5	0.3	1.1
RI10-12d	201	1105	485	1199	193	1027	219	17	248	200	123	15	9	90	63	0.2	80.0	0.5	0.6	1.1
RI10-13-a	357	1128	513	3933	173	939	202	21	228	172	50	8	3	13	4	0.3	508.9	0.5	0.3	1.2
RI10-13-c	399	1149	607	1649	239	1169	255	28	268	215	69	9	7	14	4	0.3	180.1	0.5	0.3	1.2
RI10-5	322	931	499	1369	181	1105	225	24	228	169	56	7	2	15	5	0.3	182.7	0.5	0.3	1.3
RI10-7	396	1123	739	1701	234	1222	243	27	266	203	66	9	2	18	7	0.4	182.7	0.6	0.3	1.2
RI10-8a	359	1015	519	1523	230	1116	240	27	305	227	66	10	3	13	4	0.4	160.3	0.5	0.3	1.1
RI10-8b	342	1024	547	1341	212	1059	238	23	258	193	61	8	2	13	4	0.3	161.8	0.5	0.3	1.2
RI9-1	278	1041	543	1284	201	1134	235	25	278	223	70	10	4	16	4	0.3	128.5	0.5	0.3	1.1
RI9-2	356	996	574	1556	201	1047	229	26	264	197	60	8	2	15	6	0.4	190.5	0.5	0.3	1.2
RI9-2	356	996	574	1556	201	1047	229	26	264	197	60	8	2	15	13	0.4	190.5	0.5	0.3	1.2
RI9-3	363	968	536	1477	203	1122	234	26	254	191	57	8	2	16	5	0.4	177.9	0.5	0.3	1.2
RI9-10-3	363	968	536	1477	203	1122	234	26	254	191	57	8	2	16	13	0.4	177.9	0.5	0.3	1.2
RI9-11a	394	948	711	1801	220	1066	191	24	200	159	54	8	2	22	9	0.4	233.7	0.7	0.3	1.2
RI9-11a	394	948	711	1801	220	1066	191	24	200	159	54	8	2	22	18	0.4	233.7	0.7	0.3	1.2
RI9-11b	356	780	573	1526	200	1018	181	22	187	151	50	7	2	20	8	0.5	224.6	0.6	0.3	1.2
RI9-11b	356	780	573	1526	200	1018	181	22	187	151	50	7	2	20	16	0.5	224.6	0.6	0.3	1.2
RI9-12-1	364	1070	517	1381	192	1042	229	27	241	201	59	9	2	21	8	0.3	158.9	0.5	0.3	1.1
RI9-12-1	350	1039	507	1370	191	1048	227	26	233	194	57	8	2	21	17	0.3	161.8	0.5	0.3	1.2
RI9-12-2	377	963	548	1342	200	951	214	26	240	178	57	8	2	16	6	0.4	171.5	0.6	0.3	1.2
RI9-12-2	375	966	564	1405	207	991	221	27	251	185	57	8	2	16	13	0.4	175.2	0.6	0.3	1.2
RI9-12-3	391	812	454	1182	179	864	184	22	210	157	48	7	2	8	3	0.5	170.7	0.5	0.3	1.2
RI9-12-3	390	843	460	1195	182	881	192	23	230	173	49	7	2	8	6	0.5	169.3	0.5	0.3	1.1
RI9-15-1	377	1260	684	2294	242	1298	272	29	289	225	70	10	3	16	6	0.3	226.7	0.5	0.3	1.2
RI9-15-1	371	1274	692	1727	243	1293	270	29	289	225	72	10	3	16	13	0.3	170.4	0.5	0.3	1.2
RI9-15-2	352	1075	554	1554	213	1205	258	27	287	210	67	9	2	12	4	0.3	170.5	0.5	0.3	1.2
RI9-15-2	352	1075	554	1554	213	1205	258	27	287	210	67	9	2	12	10	0.3	170.5	0.5	0.3	1.2
RI9-15-3	361	1003	511	1348	177	981	219	25	247	195	59	8	2	13	4	0.4	163.1	0.5	0.3	1.1
RI9-15-3	361	1003	511	1348	177	981	219	25	247	195	59	8	2	13	11	0.4	163.1	0.5	0.3	1.1
RI9-3	395	1154	584	1529	232	1201	269	28	288	230	69	10	2	16	5	0.3	153.1	0.5	0.3	1.2
RI9-3	395	1154	584	1529	232	1201	269	28	288	230	69	10	2	16	13	0.3	153.1	0.5	0.3	1.2
RI9-6-1	351	1070	570	1371	198	986	230	27	254	215	65	9	1	15	5	0.3	154.1	0.6	0.3	1.1
RI9-6-1	351	1070	570	1371	198	986	230	27	254	215	65	9	1	15	13	0.3	154.1	0.6	0.3	1.1
RI9-7-1	357	1146	586	1479	202	1163	253	27	304	222	68	10	2	14	4	0.3	152.2	0.5	0.3	1.1
RI9-7-1	361	1159	580	1465	200	1165	254	27	297	223	69	10	2	14	12	0.3	151.7	0.5	0.3	1.1